

## Three-dimensional shear velocity structure of the Mauléon and Arzacq Basins (Western Pyrenees)

Maximilien Lehujeur<sup>1,2,\*</sup>, Sébastien Chevrot<sup>1</sup>, Antonio Villaseñor<sup>3</sup>, Emmanuel Masini<sup>4,5</sup>,  
Nicolas Saspiturry<sup>6</sup>, Rodolphe Lescoutre<sup>7</sup>, Matthieu Sylvander<sup>8</sup> and The Maupasacq Working Group<sup>a</sup>

<sup>1</sup> GET, UMR 5563, Observatoire Midi Pyrénées, Université Paul Sabatier, CNRS, IRD, Toulouse, France

<sup>2</sup> Université Gustave Eiffel, Allée des Ponts et Chaussées, Route de Bouaye, CS 5004, 44344 Bouguenais Cedex, France

<sup>3</sup> Barcelona Center for Subsurface Imaging, Institute of Marine Sciences, ICM-CSIC, 08003 Barcelona, Spain

<sup>4</sup> M&U SASU, 3 rue des Abattoirs, 38120 Saint-Égrève, France

<sup>5</sup> ISTerre, Université de Grenoble, CS 40700, 38058 Grenoble Cedex 9, France

<sup>6</sup> Université Bordeaux Montaigne EA 4592 Géoresources et Environnement, 1 allée Fernand Daguin, 33607 Pessac Cedex, France

<sup>7</sup> Uppsala University, Department of Earth Sciences, Villavägen 16, 752 36 Uppsala, Sweden

<sup>8</sup> IRAP, UMR 5277, Observatoire Midi Pyrénées, Université Paul Sabatier, CNRS, Toulouse, France

Received: 27 January 2021 / Accepted: 24 September 2021 / Publishing online: 20 October 2021

**Abstract** – We present a 3-D shear wave velocity model of the Mauléon and Arzacq Basins from the surface down to 10 km depth, inverted from phase velocity maps at periods between 2 and 9 s. These phase velocity maps were obtained by analyzing coherent surface wave fronts extracted from ambient seismic noise recorded by the large-N Maupasacq seismic array with a matched filtering approach. This new model is in good agreement with a local earthquake tomography study performed on the same acquisition dataset. Our passive imaging models reveal the upper crustal architecture of the Mauléon and Arzacq Basins, with new details on the basement and its relationship with the overlying sedimentary cover. Combining these new tomographic images with surface and subsurface geological information allows us to trace major orogenic structures from the surface down to the basement. In the basin, the models image the first-order basin architecture with a kilometeric resolution. At depth, high velocity anomalies suggest the presence of dense deep crustal and mantle rocks in the hanging wall of north-vergent Pyrenean Thrusts. These high velocity anomalies spatially coincide with a positive gravity anomaly in the western Mauléon Basin. In addition, our models reveal major changes from the Chaînons Béarnais to the western Mauléon Basin across a set of orogen-perpendicular structures, the Saison and the Barlanès transfer zones. These changes reflect the along-strike variation of the orogenic evolution that led to the preservation of the former rifted domain and its underlying mantle in the orogenic wedge of the Western Pyrenees. We discuss the implications of these results for the 3-D architecture of the Mauléon Basin and its underlying basement.

**Keywords:** Pyrenees / seismic tomography / sedimentary basins / 3-D architecture

**Résumé** – **Structure tridimensionnelle des vitesses de cisaillement dans les bassins de Mauléon et Arzacq (Pyrénées occidentales).** Nous présentons un modèle 3-D de vitesse des ondes de cisaillement des bassins de Mauléon et d'Arzacq de la surface jusqu'à 10 km de profondeur inversé à partir de cartes de vitesse de phase pour des périodes entre 2 et 9 s. Ces cartes ont été obtenues à partir de l'analyse de fronts d'onde de surface cohérents extraits du bruit sismique ambiant enregistré par le réseau Maupasacq par filtrage adaptatif. Ce nouveau modèle est en bon accord avec la tomographie locale réalisée sur ce même jeu de données. Nos nouvelles images tomographiques révèlent l'architecture supra-crustale des bassins de

\*Corresponding author: [maximilien.lehujeur@univ-eiffel.fr](mailto:maximilien.lehujeur@univ-eiffel.fr)

<sup>a</sup>The Maupasacq Working Group includes the authors and Magali Collin (Total), Sylvain Calassou (Total), Marc Martin (Total), Adnand Bitri (BRGM), Martin Rolland (CNRS), Laurent Stehly (ISTerre), Jacques Brives (ISTerre), Pierre Boué (ISTerre), Philippe L'Excellent (CNRS), Nikos Martakis (Seismotech), Jordi Diaz (CSIC), Stephen Beller (OMP), Frank Grimaud (OMP), Katerina Polychronopoulou (Seismotech), Maik Neukirch (CSIC), Juvenal Andres Cabrera (CSIC), Georgios Christaras (Seismotech), Ayman Morouj (Seismotech), Boris Boin (CNRS), Sébastien Benhamed (OMP), Paula Romero Lopez (CSIC), Christoforos Tournazatos (Seismotech), Konstantinos Fragiadakis (Seismotech), Laurie Chopard (CNRS) and Julie Clemente (CNRS).

Mauléon et d'Arzacq, avec des informations nouvelles sur la nature du socle et sa relation à la couverture sédimentaire. En combinant ces nouvelles images tomographiques aux informations géologiques, il est possible de tracer les principales structures orogéniques de la surface jusqu'au socle des bassins. Dans le bassin, les modèles nous fournissent une image de premier ordre des plis et chevauchements à l'échelle kilométrique. En profondeur, les anomalies rapides suggèrent la présence de roches de la croûte inférieure et du manteau dans le toit des chevauchements pyrénéens de pendage nord. Ces anomalies rapides coïncident spatialement avec l'anomalie gravimétrique positive dans la partie ouest du bassin de Mauléon. Nos modèles tomographiques documentent également des changements de structures majeurs entre les Chaînes Béarnais et la partie ouest du bassin de Mauléon à travers des structures perpendiculaires à l'axe de la chaîne, représentées par les structures transverses du Saison et du Barlanès. Ce changement structural reflète les variations latérales de l'évolution orogénique qui a conduit à la préservation des domaines de rift hyper-étirés et du manteau sous-jacent dans le prisme orogénique. Nous discutons les implications de ces résultats concernant l'architecture 3-D du bassin de Mauléon et du socle sous-jacent.

**Mots clés** : Pyrénées / tomographie sismique / bassins sédimentaires / structure 3-D

## 1 Introduction

Imaging crustal structures with a fine spatial resolution is an important goal of modern seismology, with major implications in domains such as georesources and seismic hazard. In regions where strong crustal heterogeneity prevails, such as in orogens, passive imaging using local earthquakes remains challenging owing to the uneven distribution of seismicity, both in time and space, and to the sparsity of permanent seismic networks. With ambient seismic noise, seismologists can now reconstruct surface waves from pairs of seismic stations, thereby freeing themselves from relying on the occurrence of natural earthquakes (*e.g.*, Shapiro *et al.*, 2005). Ambient noise surface wave tomography (SWT) has gained a large interest in the academic world and have been applied to a very broad range of scales and contexts. Most studies focused on large scale applications like North America (*e.g.*, Lin *et al.*, 2008) or Europe (*e.g.*, Lu *et al.*, 2018). The extension of the method at a regional scale using lower periods (below 10 s) are often very efficient to image the contours of the sedimentary basins, usually characterized by lower velocities (*e.g.*, Macquet *et al.*, 2014). Fewer studies have focused on the use of surface waves from the ambient seismic noise to image structures inside a sedimentary basin (Jia and Clayton, 2021 being a recent exception). The advantages related to this passive source of seismic waves *i.e.*, continuity of sources and reduced acquisition costs compared to active seismic methods, did however motivate focused applications on sedimentary basins for example for the characterization of an oil and gas field (*e.g.*, Mordret *et al.*, 2013), the subsurface imaging for the exploration of deep geothermal resources (*e.g.*, Lehujeur *et al.*, 2018; Planès *et al.*, 2019) or the monitoring of CO<sub>2</sub> underground storage sites (*e.g.*, Gassenmeier *et al.*, 2014). Another recent advance came from the recognition that large-N node deployments such as those commonly used in controlled-source acquisitions for the oil and gas industry provide rich and valuable datasets for passive imaging studies (*e.g.*, Schmandt and Clayton, 2013). These two recent developments have opened important new perspectives not only for crustal-scale tomography, but also to get valuable insights on the 3-D geometry of sedimentary basins in structurally complex areas to complement active seismic reflection surveys.

To investigate the potential of passive imaging for the characterization of sedimentary basins, which has so far received little attention from the academic world, we have deployed a large-N array of 442 sensors, the Maupasacq experiment, in the western part of the Northern Pyrenees foothills, from March to September 2017. The inner part of the network formed a regular 50 × 30 km rectangular grid, extended to about 120 × 130 km, thanks to two additional circular deployments (Fig. 1). In the inner rectangular grid, the station spacing ranged from 1 km between the geophone nodes to 7 km between the broadband stations (details in Polychronopoulou *et al.*, 2018; Lehujeur and Chevrot, 2020). The acquisition covers the Mauléon and Arzacq Basins with 191 geophone nodes, 197 short period instruments, and 54 broadband stations. Despite being widely covered by seismic reflection profiles and wells, thanks to decades of oil and gas exploration, the 3-D architecture of the Mauléon-Arzacq Rift System remains poorly constrained.

Different rift phases are regionally recognized during the Mesozoic, but it is well accepted that the north Pyrenean Rift Basins are mostly shaped by the Aptian-Cenomanian hyper-extension rifting stage before being shortened by the Pyrenean orogenesis from Late Cretaceous onwards. The structural complexity resulting from this polyphasic deformation history probably explains why active deep reflection seismic techniques failed to image even the first-order geometry of the basins (Daignières *et al.*, 1994). This area is also characterized by a major positive gravity anomaly regionally known as the Labourd anomaly (Casas *et al.*, 1997; Chevrot *et al.*, 2014) (Figs. 2A and 2C), which has been recently related to the presence of a mantle body in the basement of the northern part of the Mauléon Basin (*e.g.*, Jammes *et al.*, 2009; Masini *et al.*, 2014; Wang *et al.*, 2016; Saspiturry *et al.*, 2019b; Lescoutre and Manatschal, 2020) (Fig. 2D). In spite of its importance to understand the rifting and orogenic evolutions, the 3-D morphology of the continental Moho beneath the study area remains disputed (Daignières *et al.*, 1994; Chevrot *et al.*, 2015; Wang *et al.*, 2016; Teixell *et al.*, 2018).

In this work, we exploit phase velocity maps of fundamental mode Rayleigh waves at periods between 2 and 9 s in order to invert a 3-D shear wave velocity ( $V_S$ ) model of the area. These phase velocity maps were obtained by extracting coherent surface wave fronts from seismic noise

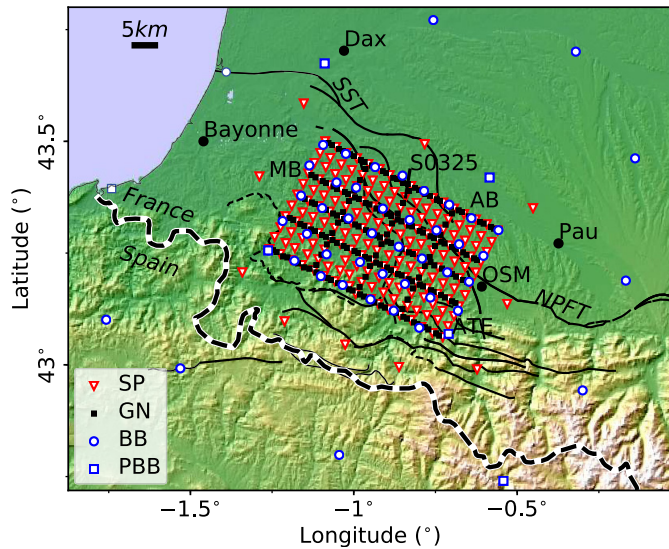


**Fig. 1.** Map of stations (SP: short period; GN: Geophone nodes; BB: broadband; PBB: permanent broadband) deployed during the Maupasacq experiment. OSM: Oloron-Sainte-Marie; AB: Arzacq Basin; MB: Mauléon Basin; NPFT: North Pyrenean Frontal Thrust; SST: Sainte-Suzanne Thrust. The solid lines indicate some of the known faults of the area, the thin dashed line SW of the survey indicates the contact between the Labourd Paleozoic basement and the sediments of the Mauléon Basin and its equivalent along the Arbailles Massif further to the south, see Figure 2B. The thick dashed line delimits the French-Spanish border.

originating from the Atlantic and Mediterranean sea using the Maupasacq array, as described in Lehujeur and Chevrot (2020). The method used an innovative matched-filtering technique to exploit the large number of seismological stations deployed simultaneously on the field and the strong directivity of ambient seismic noise. The present contribution can be seen as a continuation of that work as we invert the previously obtained phase velocity maps to image the 3-D variations of shear velocity beneath the Mauléon and Arzacq Basins. The inversion procedure involves a first point-wise Markov chain Monte-Carlo inversion (MCMC) to determine a 1-D shear velocity model at each surface node of the 3-D tomographic grid. Then, these 1-D models are aggregated to get a preliminary 3-D model. This model is finally used to initiate a new 3-D iterative inversion, using a 3-D Gaussian model covariance matrix. This allows us to obtain a smooth 3-D model that fits the dispersion data.

The paper is organized as follows. In Section 2, we provide an overview of the geological context of the study area highlighting the main questions that remain concerning the architecture of the Mauléon Basin and its underlying basement. In Section 3, we describe the details of the two-step surface-wave inversion method. In Section 4, we confront and compare our  $V_S$  model derived from surface waves to other tomographic studies covering the area, and in particular to a recent local travel-time tomography that exploited the Maupasacq dataset. We also compare these models to constrained geological information from geological maps and well data. Finally, in Section 5 after discussing the limits of

passive imaging approaches, we propose a 3-D geological interpretation of the tomographic models.

## 2 Geological setting

### 2.1 Present-day Pyrenean structure

The Pyrenean Mountain Belt results from the north-south convergence between the Iberian and Eurasian plates from the Late Santonian to the Early Miocene (Puigdefàbregas and Souquet, 1986; Olivet, 1996; Rosenbaum *et al.*, 2002; Macchiavelli *et al.*, 2017; Van Hinsbergen *et al.*, 2020). In its western part, the focus of this study, the belt is made of different structural units characterized by orogenic and pre-orogenic rift-related geological records (see Fig. 2B). The southern limit of the Aquitaine Foreland Basin is the North Pyrenean Frontal Thrust (NPFT), which corresponds to the Sainte-Suzanne Thrust in its westernmost part. Southward, the North Pyrenean Zone (NPZ) is separated from the Axial Zone (AZ) by the south-verging Lakhoura Thrust System. The AZ represents a large outcrop of exhumed pre-Mesozoic rocks that hold some of the highest altitudes of the Pyrenees. It is connected to the South Pyrenean Foreland Basin (SPFB) by a set of south-verging thrusts. While the AZ and the SPFB mainly result from the Eocene-Miocene antiformal nappet-stacking of pre-orogenic Iberian thick continental crust (proximal margin domains of Masini *et al.* (2014), Tugend *et al.* (2014) and Tugend *et al.* (2015)), the NPZ primarily results from the shortening of Cretaceous hyper-extended rift basins, with a basement-cover decoupling in the Upper Triassic evaporite layers. In the Western Pyrenees, the NPZ results from the inversion of the Mauléon Basin that has been thrust on top of the Aquitaine Foreland Basin. At the front of the NPFT, and buried underneath syn-orogenic sediments, the Arzacq Rift Basin corresponds to the northern extension of the Cretaceous Pyrenean Rift System that escaped from most of the orogenic overprint (Masini *et al.*, 2014; Tugend *et al.*, 2015; Angrand *et al.*, 2018; Issautier *et al.*, 2020; Ducoux *et al.*, 2021).

### 2.2 Tectono-stratigraphic evolution of the Western Pyrenees

In the Western Pyrenees, the crustal basement is made of a complex lithological assemblage of pre-Mesozoic rocks. It includes metamorphic and sedimentary rocks that were variably affected by Variscan orogenic to post-orogenic deformations and intrusions (*e.g.*, Saspiturry *et al.*, 2019a). This complex inherited crust was eroded and peneplained before being unconformably covered by continental clastics (Permian and Lower Triassic). An ill-defined early phase of rifting (see Leleu *et al.*, 2016, for a review) was recorded through the Triassic marine transgression that eventually led to the deposition of the Upper Triassic evaporites (Curnelle, 1983), which will represent the main *décollement* level during the subsequent rifting and orogenic deformations.

During the Jurassic, the Pyrenean domain recorded a quiet tectonic period through the development of a shallow marine carbonate platform (Canérot, 2017). Another ill-defined pulse of rifting, responsible for local emersion and erosion of the

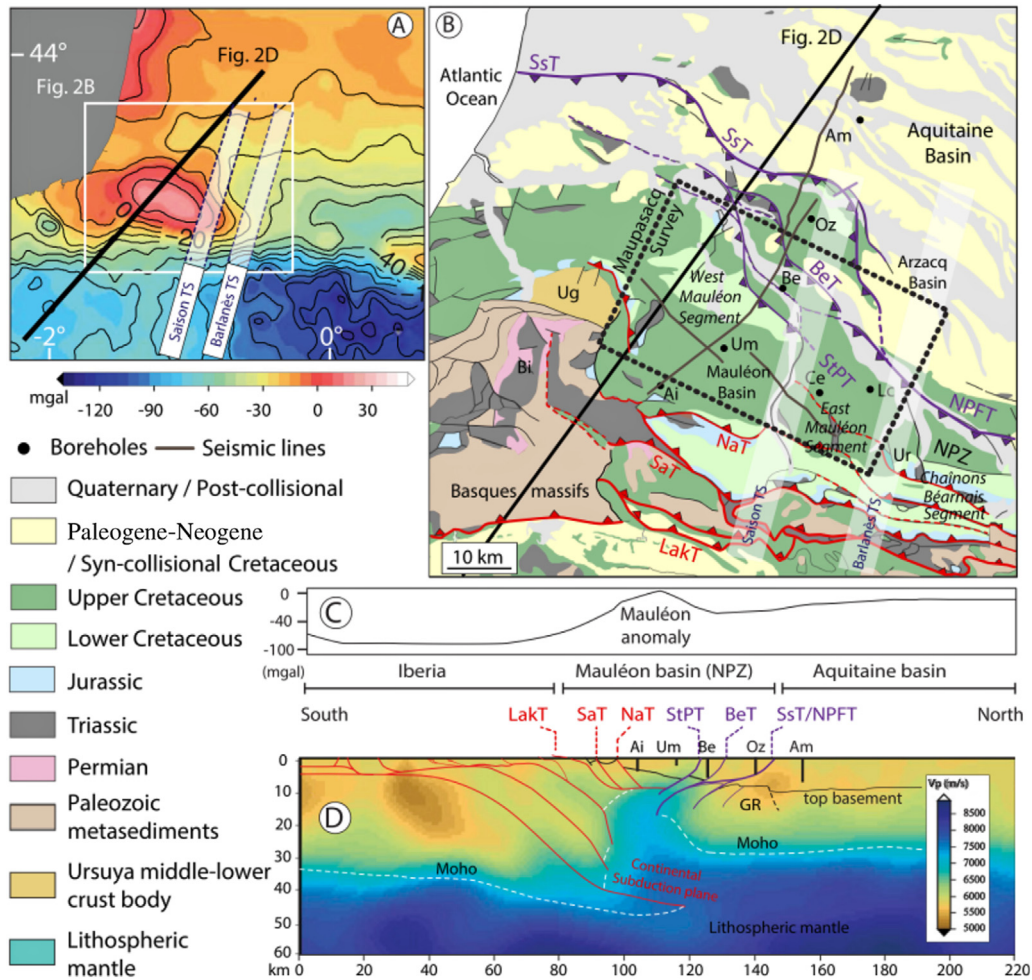


**Fig. 2.** Geological setting. (A) Bouguer gravity map of the western part of the Pyrenean Belt (Casas *et al.*, 1997), displaying a positive anomaly right upon the inverted hyperextended domain of the Mauléon Basin. Dark line: location of the Wang *et al.* (2016)  $V_p$  model of subplot D. Contour intervals are 10 mgal. (B) Geological map illustrating the Mauléon Basin pop-up structure (Saspiturry, 2019, modified from). Main south-vergent thrust faults underlined in red, match from north to south with the North Arbaillies Thrust (NaT), South Arbaillies Thrust (SaT), and the Lakhoura Thrust (LaKT). Main north-vergent thrust faults are represented in purple and correspond from south to north to the Saint-Palais Thrust (St-PT), Bellevue Thrust (BeT) and the Sainte-Suzanne Thrust (SsT) representing the western termination of the North Pyrenean Frontal Thrust (NPFT). The white shaded bands oriented N20° indicate the Saison and Barlanès transverse structures (TS) discussed in the text. Seismic reflection profiles in dark grey have been used to calibrate the uppermost and northern part of the Saspiturry *et al.* (2020b) Mauléon Basin section shown in subplot D. Ug: Ursuya granulites; Bi: Bidarray Permian Basin; Ur: Urdach mantle outcrop. Boreholes: Ai: Ainhice; Am: Amou; Be: Bellevue; Oz: Orthez; Um: Uhart-Mixe; Ce: Cheraute; Lc: Les Cassières; GR: Grand Rieu High. (C) Mauléon Basin Bouguer anomaly profile (Casas *et al.*, 1997). (D) P-wave crustal model by Wang *et al.* (2016) with superimposed interpretation by Saspiturry *et al.* (2020b).

sedimentary cover, is regionally recorded during the Late Jurassic and Early Cretaceous in the area (*e.g.*, Canérot *et al.*, 1999). The last and most intense rifting phase, the so-called hyper-extension phase, then occurred between the Aptian and the Cenomanian. As the pre-orogenic crustal and basin architectures are mainly shaped by this hyper-extension phase of rifting, we will consistently refer to this latter phase by using a pre-, syn- and post-HE terminology (“HE” standing for “hyper-extension”) to avoid any confusion with preceding rifting phases. While the precise kinematics of hyper-extension is still debated, it corresponds to the main phase of crustal thinning and accelerated subsidence within the Mauléon and Arzacq Basins. Within the Mauléon Basin, this hyper-extension phase eventually led to the exhumation of the subcontinental

mantle at the seafloor during the Early Cenomanian (Fig. 2D; Jammes *et al.*, 2009; Masini *et al.*, 2014; Saspiturry *et al.*, 2019b) and to the rework of mantle clasts within the syn-HE sediments (Fortané *et al.*, 1986; Jammes *et al.*, 2009; Lagabrielle *et al.*, 2010; Debros *et al.*, 2010; Corre *et al.*, 2016; Asti *et al.*, 2019; Lagabrielle *et al.*, 2019). Crustal thinning and tectonic exhumation of mantle rocks were proposed to be accommodated by a set of long-offset detachment faults dipping either to the north, to the south, or both, depending on the authors (Jammes *et al.*, 2009; Masini *et al.*, 2014; Gómez-Romeu *et al.*, 2019; Saspiturry *et al.*, 2019b, Lescoutre *et al.*, 2019).

After a short post-rift relaxation until the Late Santonian, early orogenesis initiated with the inversion of the Mauléon

Basin forming the early orogenic fold-and-thrust belt of the Western Pyrenees. During this stage, deformation was accommodated by the underthrusting of the former hyper-thinned continental and exhumed mantle basement of the Mauléon Basin underneath the European continental crust (Tugend *et al.*, 2014; Mouthereau *et al.*, 2014; Gómez-Romeu *et al.*, 2019). At the surface, part of the pre-HE sedimentary cover together with the syn- and post-HE cover were detached from the hyper-extended basement (including Permian and Lower-Middle Triassic rocks) using the Keuper evaporites as a basal *décollement* level. The Lakhora and NPFT Fault Systems thrust the deformed sedimentary cover on top of both the Iberian and European continents (Jammes *et al.*, 2009; Teixell *et al.*, 2016; Labaume and Teixell, 2020). Following a Paleocene transitional phase of more diffuse deformations (the “Pyrenean tectonic quiescence”) and a Lower Eocene proto-collision stage (for details, see Teixell *et al.*, 2016; Waldner *et al.*, 2021), shortening propagated further south from the Eocene to the Miocene and formed the Pyrenean Axial Zone and the Iberian Foreland fFold and Thrust Belt (the South Pyrenean Zone) up to the pro-foreland basin (the Ebro Basin). While the collisional flexure was also recorded on the European retro-foreland basin, shortening rates were more limited there in comparison to the southern side of the belt (e.g., Waldner *et al.*, 2021; Teixell *et al.*, 2016; Angrand *et al.*, 2018). In the study area, syn-collisional deposits are lying underneath and northwards of the NPFT (*i.e.*, in the Aquitaine/Arzacq Basins) as turbiditic deposits grading upsection to syn- and post-orogenic marine and continental clastics. At depth, shortening was accommodated by the north-directed underthrusting of the Iberian crust beneath Europe leading to the present-day imaged geometry of the crustal root (Wang *et al.*, 2016; Chevrot *et al.*, 2018) (Fig. 2D).

### 2.3 The non-cylindrical structure of the Western Pyrenees

As introduced above, the structure of the NPZ and southern Aquitaine Basin is mostly related to the inversion of the Mauléon hyper-extended rift system. 2-D geological models generally state that the thin-skinned shortening style recorded within the NPZ results from the decoupling created by the evaporitic *décollement*, above which the cover got passively squeezed in a pop-up structure while the basement was thickened by thrusts (Tugend *et al.*, 2014; Mouthereau *et al.*, 2014; Dumont *et al.*, 2015; Teixell *et al.*, 2016; Labaume and Teixell, 2020). If this evolution fits with first order observations in the eastern part of the Mauléon Basin, sections and models proposed for the western side of the study area rather advocate a thick-skin crustal pop-up that sampled the autochthonous basement of the Mauléon Basin within the orogenic wedge (e.g., Jammes *et al.*, 2009; Masini *et al.*, 2014; Lescoutre and Manatschal, 2020; Saspiturry *et al.*, 2020a). This pop-up structure is edged by the lateral continuations of the Lakhora and NPFT systems in the south and north, respectively (Teixell *et al.*, 2016; Lescoutre *et al.*, 2021; Lescoutre and Manatschal, 2020; Saspiturry *et al.*, 2020a; Fig. 2D). It should be noticed that the sampled basement is outcropping within the Basque Massif forming the south-western margin of the Mauléon Basin (Fig. 2B). There, it is

made of Paleozoic rocks (with its pre-Keuper cover) to the south and of the Ursuya granulites to the north, the latter bearing a small body of serpentinized mantle (Boissonnas *et al.*, 1974; Vielzeuf and Kornprobst, 1984; Masini *et al.*, 2014; Lescoutre, 2019; Saspiturry *et al.*, 2019a, 2019b). The pre-orogenic sediment draping of these basement rocks suggests that it corresponds to the autochthonous basement of the Mauléon Basin, made of thinned continental crust and mantle rocks (Jammes *et al.*, 2009; Masini *et al.*, 2014; Wang *et al.*, 2016; Chevrot *et al.*, 2018; Lescoutre *et al.*, 2021; Saspiturry *et al.*, 2020a). The Labourd positive gravity anomaly in the western part of the Mauléon Basin gives further support to this hypothesis (Figs. 2A and 2C). Although this anomaly was initially attributed to the presence of lower crustal rocks at shallow depth (Grandjean, 1994; Vacher and Souriau, 2001; Pedreira *et al.*, 2007), it has also been interpreted as a shallow piece of dense lithospheric mantle (Casas *et al.*, 1997; Jammes *et al.*, 2010). This interpretation has gained support from recent works documenting P-wave velocities of 7.3 km/s below 10 km depth (Fig. 2D; Wang *et al.*, 2016; Chevrot *et al.*, 2018). It was also observed that this gravity anomaly is progressively attenuating from west to east (Gottis, 1972; Boillot *et al.*, 1973, Fig. 2A), suggesting a structural and/or a lithological change across the basin (e.g., Masini *et al.*, 2014; Fig. 2A). Lescoutre and Manatschal (2020) recently explained this structural change as reflecting the transition between shifted Mauléon-Arzacq and Basque-Cantabrian Rift Axes located north-east and south-west, respectively, of the Basque Massif (Fig. 2B). In this model the N20° orogen-perpendicular Saison and Barlanès transverse structures (TS; Rat, 1988; Razin, 1989; Masini *et al.*, 2014; Saspiturry, 2019; Lescoutre *et al.*, 2021; Fig. 2B) played a significant role on the non-cylindrical structure of the Mauléon Basin. These structures divide the study area in 3 segments from west to east: the western and eastern Mauléon segments, and the Chaînons Béarnais segment (Fig. 2B). The Saison structure is characterized by a steep dipping dextral shear zone (Zolnai, 1975; Schoeffler, 1982; Richard, 1986; Saspiturry, 2019), whereas the Barlanès structure corresponds to the lateral termination of the Chaînons Béarnais folds. Even though they are assumed to be of fundamental importance for the closure of rifted domains during orogenesis (e.g., Lescoutre and Manatschal, 2020; Saspiturry, 2019), their precise geometry and role at depth remain to be precised, which was one of the main motivations in the choice of the emplacement of the Maupasacq seismic acquisition used in this study.

## 3 Methods

### 3.1 Surface wave tomography

The inversion of surface wave dispersion curves to determine the vertical variations of elastic parameters (density, shear and compressional wave velocities) is a classical non-linear inverse problem commonly encountered in earthquake or ambient noise tomography. The forward problem can be efficiently computed using the propagator matrix method, which considers a superposition of homogeneous layers over a half-space (e.g., Thomson, 1950; Haskell, 1953; Knopoff, 1964; Gilbert and Backus, 1966; Aki and Richards, 2002).

The linearization of the problem has been extensively used to invert surface wave dispersion measurements because it is computationally efficient and can rapidly converge to a solution (e.g., Dorman and Ewing, 1962; Xia *et al.*, 1999). However, the inversion results may depend on the initial model. Due to the non-uniqueness of the solution, the lack of prior knowledge about the structures can therefore lead to very different models that fit the observations equally well (e.g., Bodet *et al.*, 2005). Global search approaches such as grid search (e.g., Macquet *et al.*, 2014), Monte-Carlo methods (e.g., Shapiro and Ritzwoller, 2002; Socco and Boiero, 2008; Maraschini and Foti, 2010), genetic algorithms (e.g., Lomax and Snieder, 1994), or neighborhood algorithms (Sambridge, 1999; Mordret *et al.*, 2014) are thus often preferred since they only require solving a forward problem. In addition, they can also provide the posterior covariance matrix of the model.

Building a 3-D S-wave velocity model based on the phase velocity of surface waves is classically done by first estimating the local dispersion curves at each geographical location and then solving many independent 1-D inverse problems (e.g., Shapiro and Ritzwoller, 2002). Other studies have proposed to integrate these two inversion problems into one to determine directly the 3-D structure either by linearized or Monte-Carlo methods (Fang *et al.*, 2015; Zhang *et al.*, 2018). These techniques still rely on the 1-D approximation for the forward computation of dispersion curves, but they allow controlling the lateral coherence of the velocity parameters.

In this work, we employ another two-step inversion scheme to invert a set of surface wave dispersion maps at several periods, and we apply it to the Rayleigh waves phase velocity dispersion maps from Lehujeur and Chevrot (2020). In the first step, we invert the surface wave dispersion curves at each geographical location independently using a 1-D Markov chain Monte-Carlo inversion. This step provides us a probability density function of the S-wave velocity as a function of depth at each location. The median profiles are combined to form a preliminary 3-D S-wave velocity model. In the second step, we perform a 3-D linearized inversion starting from the result of the point-wise inversion, and we regularize the problem using a non-diagonal covariance matrix over the model space to smooth the model laterally and vertically, while preserving the fit to the dispersion data.

### 3.1.1 Preliminary point-wise depth inversion

We first determine a preliminary model following the inversion approach described in Lehujeur *et al.* (2018) except for some aspects that are detailed below. We invert the phase velocity dispersion curves of fundamental mode Rayleigh waves sampled logarithmically at 9 periods between 2 and 9 s on the surface nodes of the 3-D tomographic grid (Lehujeur and Chevrot, 2020). We assume that the phase velocity measurements at the 9 periods are independent. The 1-D models are described by the shear velocity ( $V_S$ ) and thickness of 8 homogeneous layers overlying a half-space. The  $V_P$  and density inside each layer, needed for the resolution of the forward problem are derived from  $V_S$ , using the  $V_P$ -to- $V_S$  and  $V_P$ -to-density scaling relationships given by Brocher (2005):

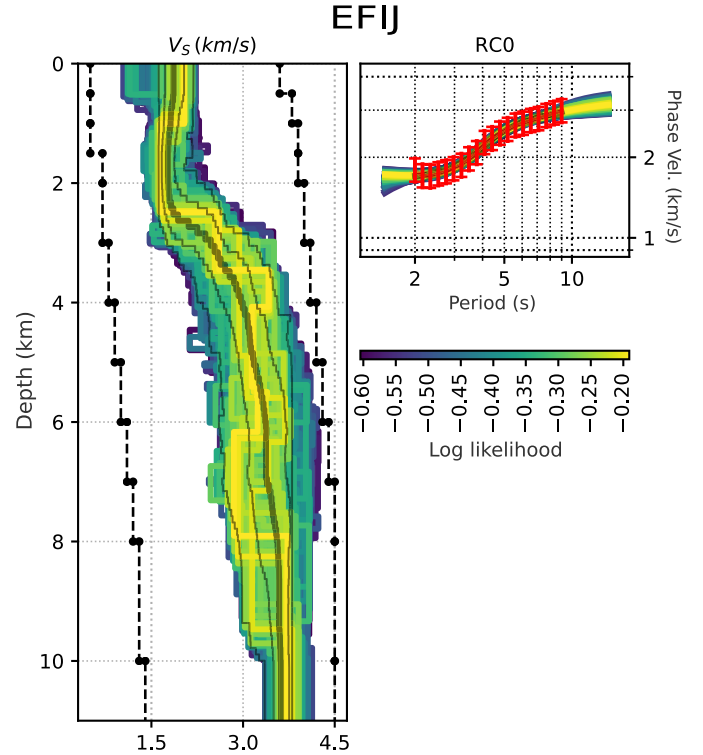


**Fig. 3.** Result of the point-wise depth inversion for the grid point located at the intersection of slices EF and IJ as indicated in Figure 5. (Left panel) Model space: the dashed black lines indicate the boundaries of the search area. The colored  $V_S$  models indicate the best 1000 models retained. The thick grey solid model indicates the median of the 1000 best models found. (Right panel) Data space: the red curve with error bars indicates the observed Rayleigh wave phase velocity dispersion data to fit. The colored dispersion curves are the projection of the 1000 best models onto the data space.

$$V_P = 0.9409 + 2.0947 V_S - 0.8206 V_S^2 + 0.2683 V_S^3 - 0.0251 V_S^4, \quad (1)$$

$$\rho = 1.6612 V_P - 0.4721 V_P^2 + 0.0671 V_P^3 - 0.0043 V_P^4 + 0.000106 V_P^5. \quad (2)$$

These relations are valid for  $V_S \leq 4.5$  km/s (Eq. (1)), and for  $1.5 \leq V_P \leq 8.5$  km/s (Eq. (2)). Here, we used them mostly to reduce the size of the model space to be explored by the Markov chain Monte-Carlo algorithm, which reduces significantly the computational effort required by the first step of our inversion procedure and does not impact the solution in a significant way as the Rayleigh waves are mostly sensitive to  $V_S$  (e.g., Xia *et al.*, 1999). The dispersion curves are computed with the codes from Herrmann (2013). All the inverted parameters are restricted to a prescribed range using a uniform probability density law, which reduces even more the size of the model space to explore and avoids testing unrealistic models (see the area delimited with black dotted lines in Fig. 3). In addition, we impose that the  $V_S$  variation between two consecutive layers are between  $-0.5$  and  $+1.0$  km/s. This additional constraint forces the tested models to remain

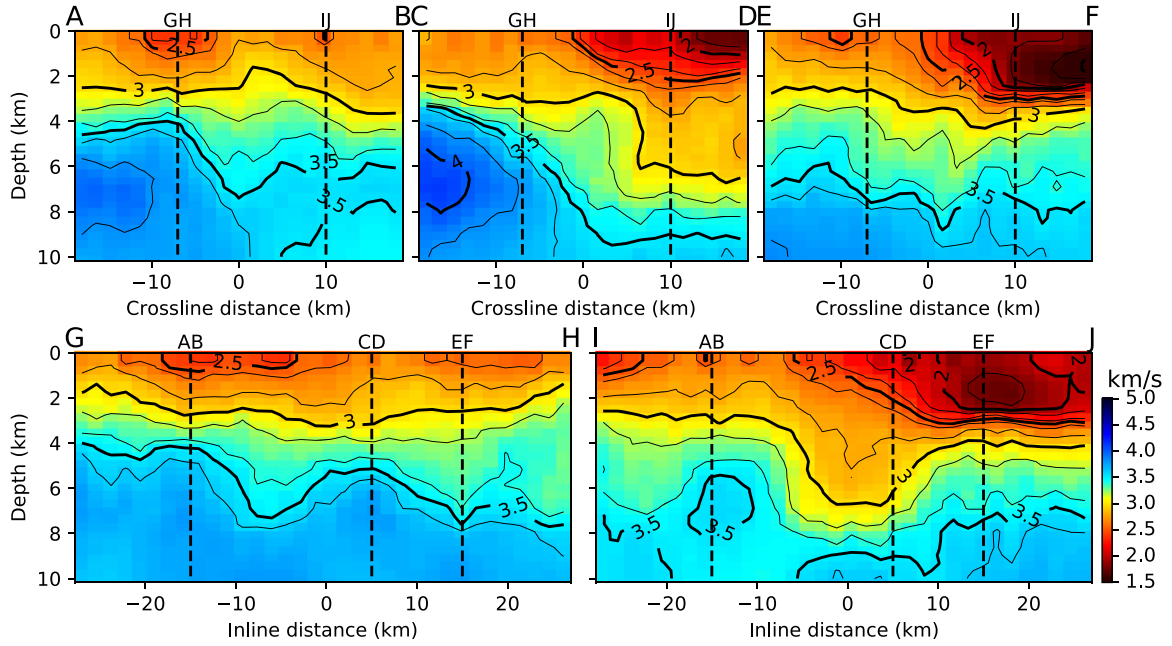


**Fig. 4.** Vertical profiles across the prior  $V_S$  model obtained from point-wise depth inversion. The location of the slices are indicated in [Figure 5](#).

relatively smooth, while still allowing the velocity to decrease with depth.

The inversions are run using 10 independent Markov chains launched in parallel. The proposal distribution is adjusted during the inversion to maintain an acceptance rate of the Metropolis algorithm around 25%, and the Markov chains run until 2500 models are kept, so that approximately 10 000 models are tested. We retain the median of the 1000 best models found as the solution of the inversion ([Fig. 3](#)). After combining all the median 1-D models, we obtained the 3-D S-wave velocity model shown in [Figures 4](#) and [5](#). The solutions at nearby locations are very consistent although the inverse problems are solved independently, which emphasizes the stability of the point-wise approach. However, the small-scale irregularities suggest that the model is noisy. A simple cure would be to smooth the model, but this would degrade the fit of observed data, as discussed later.

### 3.1.2 3-D inversion

To obtain the final 3-D  $V_S$  model, we perform a new linearized 3-D inversion, starting from the solution obtained with the point-wise inversion described in the previous section, following the method described in [Montagner and Tanimoto \(1990\)](#) for global surface-wave tomography. We regularize the problem using a non-diagonal Gaussian 3-D covariance matrix to smooth the model, while preserving the fit to the observations. The model is parameterized into a regular  $34 \times 23 \times 30$  Cartesian grid of  $1.612 \times 1.636 \times 0.345$  km size cells. As in the preliminary inversion,  $V_p$  and density are scaled to  $V_S$  using the relations from [Brocher \(2005\)](#) (Eqs. (1) and (2)). The least squares cost function to minimize is defined by [Tarantola and Valette \(1982\)](#):

$$\chi^2(\mathbf{m}_n) = \chi_d^2(\mathbf{m}_n) + \chi_m^2(\mathbf{m}_n), \quad (3)$$

where,

$$\chi_d^2(\mathbf{m}_n) = \frac{1}{2} [\mathbf{d}^{obs} - \mathbf{g}(\mathbf{m}_n)]^T \cdot \mathbf{C}_d^{-1} \cdot [\mathbf{d}^{obs} - \mathbf{g}(\mathbf{m}_n)], \quad (4)$$

$$\chi_m^2(\mathbf{m}_n) = \frac{1}{2} [\mathbf{m}_n - \mathbf{m}_0]^T \cdot \mathbf{C}_m^{-1} \cdot [\mathbf{m}_n - \mathbf{m}_0], \quad (5)$$

where  $\mathbf{d}^{obs}$  is the data vector that contains the dispersion measurements,  $\mathbf{g}$  is the operator that predicts the Rayleigh wave dispersion curves,  $\mathbf{m}_n$  is the model vector that contains the values of  $V_S$  inside each tomographic grid cell,  $n$  is the iteration number of the linearized inversion, and  $\mathbf{m}_0$  is the starting  $V_S$  model. We assume that all the measurements are independent and thus we use a diagonal data covariance matrix  $\mathbf{C}_d$ . We also assume that the spatial variations of  $V_S$  can be described by a Gaussian covariance matrix.

$$\mathbf{C}_m = \sigma_m^2 \mathbf{S}, \quad (6)$$

where  $\sigma_m$  is the prior uncertainty on the  $V_S$  model assumed homogeneous and tuned to regularize the inverse problem, and  $\mathbf{S}$  the Gaussian smoothing kernel:

$$S_{ij} = \exp \left\{ -\frac{1}{2} \left[ (\mathbf{r}_i - \mathbf{r}_j)^T \cdot \mathbf{L}^{-1} \cdot (\mathbf{r}_i - \mathbf{r}_j) \right] \right\}. \quad (7)$$

where  $\mathbf{r}_i$  is the location of cell  $i$ . Because we expect a finer vertical resolution, we impose two distinct correlation lengths along the horizontal and vertical dimensions:

$$\mathbf{L} = \begin{bmatrix} L_h^2 & & \\ & L_h^2 & \\ & & L_v^2 \end{bmatrix}, \quad (8)$$

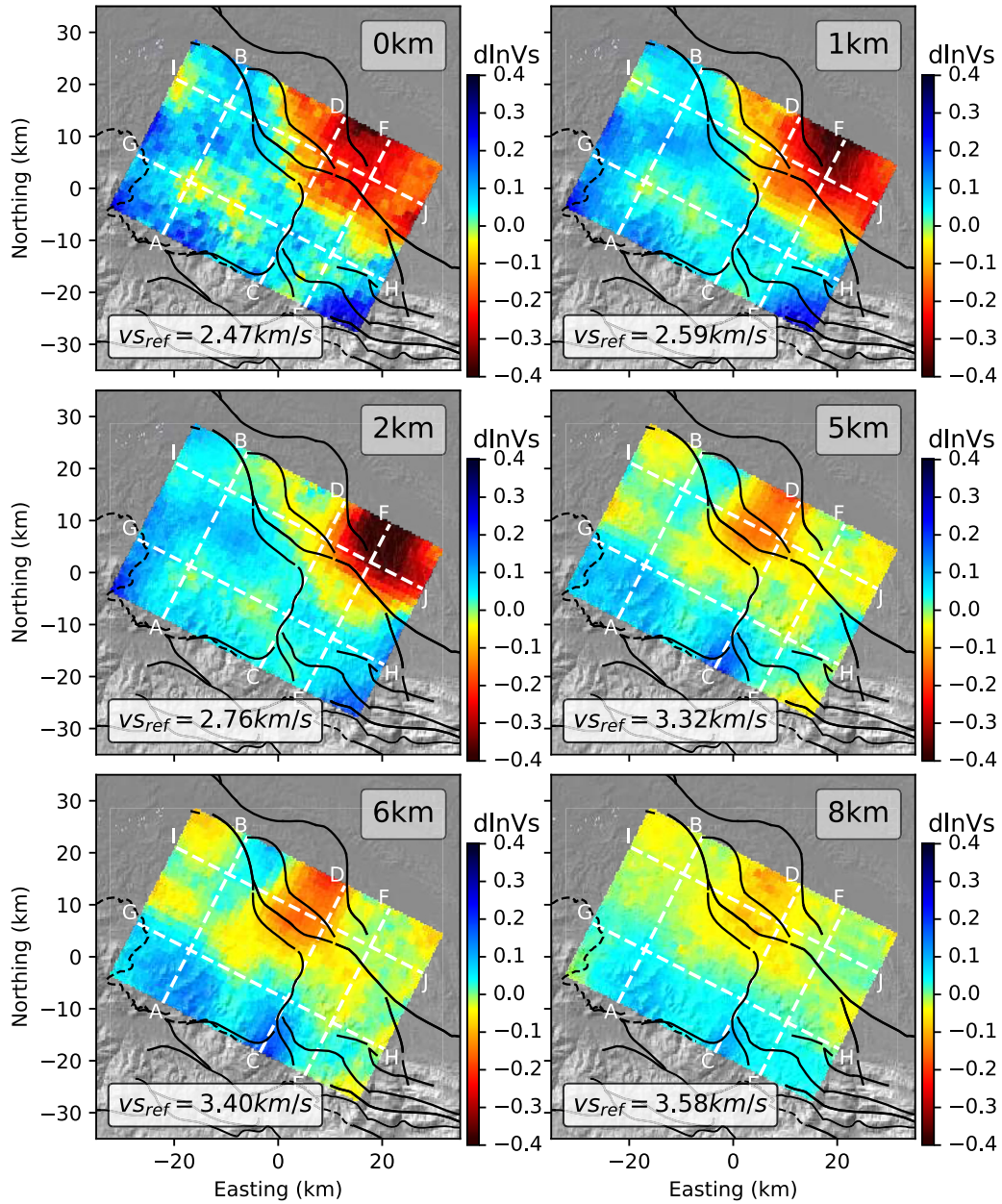


**Fig. 5.** Horizontal sections across the prior  $V_S$  model obtained from point-wise depth inversion. The black lines indicate the surface location of the main faults after [Sasipiturry \*et al.\* \(2019b\)](#).

where the horizontal ( $L_h$ ) and vertical ( $L_v$ ) correlation lengths are set to 2.5 km and 1 km, respectively.

This non-linear inverse problem is solved iteratively following [Tarantola and Valette \(1982\)](#), where the model is updated at each iteration according to:

$$\mathbf{m}_{n+1} = \mathbf{m}_0 + \mathbf{C}_m \cdot \mathbf{G}_n^T (\mathbf{C}_d + \mathbf{G}_n \cdot \mathbf{C}_m \cdot \mathbf{G}_n^T)^{-1} \cdot [\mathbf{d}^{obs} - \mathbf{g}(\mathbf{m}_n) + \mathbf{G}_n \cdot (\mathbf{m}_n - \mathbf{m}_0)], \quad (9)$$

with  $\mathbf{G}_n$  is the matrix containing the Fréchet derivatives computed in the current model  $\mathbf{m}_n$ :

$$\mathbf{G}_n(T, z) = \left. \frac{\partial c(T)}{\partial V_S(z)} \right|_{\mathbf{m}_n}, \quad (10)$$

where  $c$  denotes the phase velocity,  $V_S$  is the S-wave velocity and  $T$  and  $z$  are the period and depth, respectively.

The inversion is initiated with  $\mathbf{m}_0$ , a smoothed version of the model  $\mathbf{m}^{prior}$  obtained in the preliminary inversion:

$$\mathbf{m}_0 = \bar{\mathbf{S}} \cdot \mathbf{m}^{prior}, \quad (11)$$

where  $\bar{\mathbf{S}}_{ij} = \mathbf{S}_{ij} / \sum_k \mathbf{S}_{ik}$  is the normalized smoothing kernel. We run the second inversion step for several values of the prior uncertainty  $\sigma_m$ , used as a damping parameter. The inversion usually converges after 3 to 10 iterations depending on the damping coefficient used. The retained prior uncertainty is  $\sigma_m = 0.4$  km/s, slightly below the maximum curvature of the L-curve computed following [Hansen and O'Leary \(1993\)](#) (see the red dashed curve in [Fig. 6](#)).

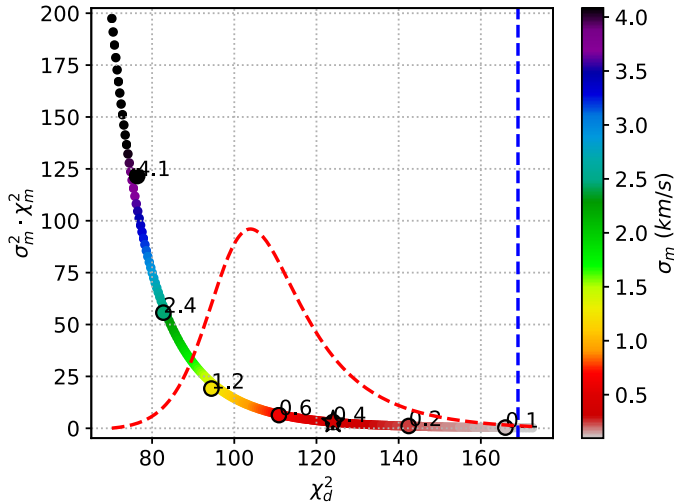


**Fig. 6.** Regularization test. The colors indicate the value of the prior uncertainty used as a damping parameter ( $\sigma_m$ ). The red dashed curve is the curvature of the L-curve. The blue dashed line indicates the data cost of the prior model from point wise depth inversion.  $\chi_d^2$  indicates the data misfit term  $\frac{1}{2} [d^{obs} - g(m)]^T \cdot C_d^{-1} \cdot [d^{obs} - g(m)]$  and  $\chi_m^2$  corresponds to the model norm  $\frac{1}{2} [m_n - m_0]^T \cdot C_m^{-1} \cdot [m_n - m_0]$ .

The data misfit (first term of Eq. (3)) obtained with the prior model resulting from point-wise inversion (step 1) is  $\chi_d^2(m^{prior}) = 169$  in arbitrary units (Fig. 6, blue dashed line). The starting model from equation (11) has a much larger data misfit  $\chi_d^2(m_0) = 465$ , which demonstrates that simply smoothing the output of a point-wise inversion deteriorates the fit to dispersion data. After convergence of the second inversion, the data misfit for  $\sigma_m = 0.4$  km/s is  $\chi_d^2(m^{sol}) = 124$  (Fig. 6), which is lower than the misfit obtained with the prior model. Examples of observed and modeled dispersion curves for the prior, starting, and optimized models are shown in Figure 7.

### 3.2 Local earthquake tomography

In order to provide independent constraints on the S-wave velocity structure, we also show the results of a  $V_S$  model obtained from local earthquake tomography (Villaseñor *et al.*, 2019), using arrival times picked on records from the stations of the Maupasacq experiment. During the 6 months of operation of this temporary network, a total of 1980 local earthquakes were detected and located (Polychronopoulou *et al.*, 2018). From this catalog, we selected for the tomography well recorded earthquakes with at least 8 P arrival times, 2 S arrival times and an azimuthal gap smaller than  $200^\circ$ . This resulted in a dataset consisting of 996 earthquakes with a total of 87 122 P-wave and 72 445 S-wave arrival times.

The tomographic inversion method used is based on Benz *et al.* (1996) as modified by Tryggvason *et al.* (2002) in order to incorporate P- and S-wave arrival times. The travel times (forward problem) are calculated using the finite-difference code of Podvin and Lecomte (1991), which provides accurate results even for models with large lateral variations in velocity structure. The tomographic method inverts simultaneously for P- and S-wave velocity structure and earthquake relocation. This is a non-linear inverse problem so in order to find its

solution it is first linearized and then solved iteratively. The model is parameterized in terms of constant velocity cells of  $1.2 \times 1.2 \times 1.2$  km in size, and the dimensions of the model region are 130 km and 115 km along the E-W and N-S directions respectively.

The starting model used in the inversion is the 1-D velocity model previously determined for earthquake location (Polychronopoulou *et al.*, 2018). The final model shown here was obtained after 10 iterations. The initial root-mean square (RMS) error of the used arrival times was 0.107 s for P-waves and 0.101 s for S-waves, and the final RMS was 0.082 s for P-waves and 0.081 s for S-waves. This represents a variance reduction of 23% for P-waves and 20% for S-waves, which is typical for travel time tomography. We estimated the resolving power of the dataset performing reconstruction tests of synthetic checkerboard models (Supplementary Material S3). Due to the high density of stations, we were able to resolve reliably anomalies of 5 km in size and larger in the center of the LET model (southern part of the Maupasacq deployment), where the high velocity anomalies of interest are located.

The S-wave velocity model obtained using local earthquake tomography shows finer details than the one obtained from SWT in the regions that are well sampled by crossing rays. However large regions of the model that are not illuminated by rays are unconstrained. This problem is less significant in surface wave tomography because of the characteristics of the sensitivity of surface waves. Similarly the actual value of the velocity anomalies obtained from local earthquake tomography is typically overestimated, while the values obtained from surface waves are more realistic. Therefore, combining the complementary characteristics of both methods we can better describe the features of the seismic velocity structure.

## 4 The tomographic models

The final  $V_S$  model obtained after inversion of the surface wave dispersion curves is shown in Figures 8 and 9. As expected, this model is smoother than the prior model shown in Figure 4 but the dominant structures are very similar. Figure 10 displays  $V_S$  at 1 km depth in our surface-wave tomography (SWT) model and in the local earthquake tomography (LET)  $V_S$  model described here and in Villaseñor *et al.* (2019). Whereas these two models were derived from completely independent datasets, they show very similar and coherent velocity structures. For example, both models image higher than average velocities in the Mauléon Basin (SW part in the map shown in Fig. 10). However, the average velocity in the LET model is clearly on average faster than in the SWT model. Figures 11–13 show cross-sections in the SWT and LET models. These vertical cross-sections are also in good agreement, but the vertical resolution is finer in the SWT model than in the LET model, especially in the area of the Arzacq Basin (Fig. 11). For example, the expected top of the basement of the Arzacq Basin (ca. 3 km in depth on the northern part of the Fig. 11) is more sharply defined in the SWT model whereas the LET model shows a more gradual transition. In contrast, the LET model has a finer lateral resolution compared to the SWT model, especially at depths larger than 6 km.

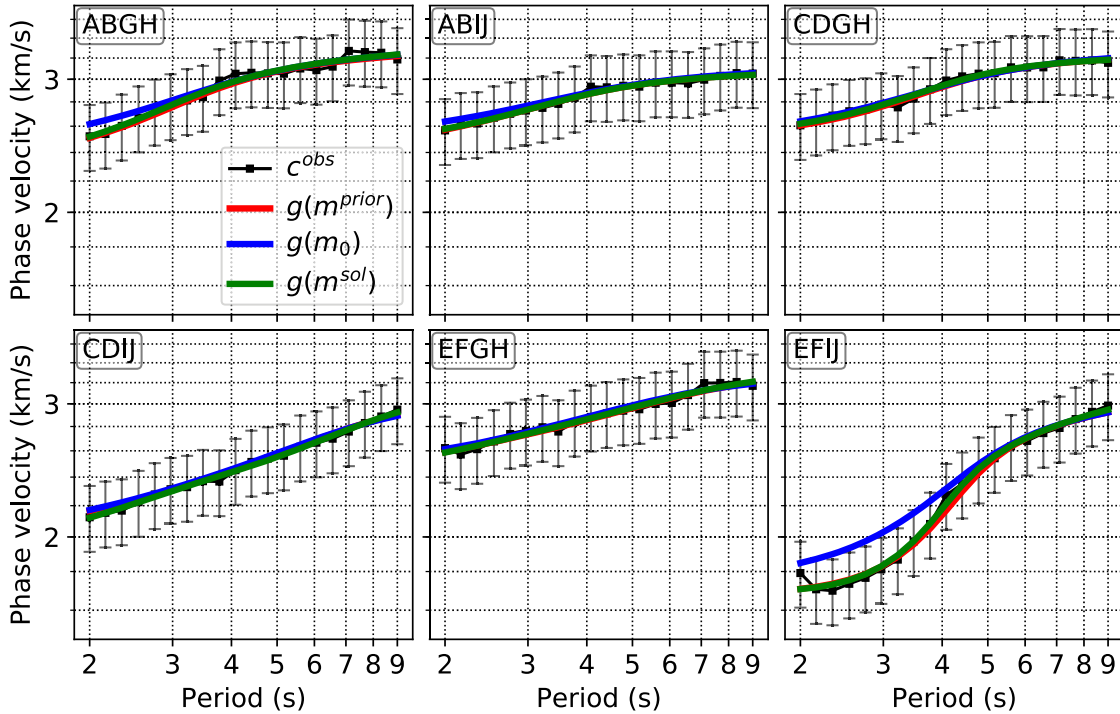


**Fig. 7.** Observed and modeled Rayleigh wave phase velocity dispersion curves at the intersection between slices AB, CD, EF, GH and IJ (see Fig. 5).  $m^{prior}$ : model obtained from the point-wise inversion (step 1).  $m_0$ : smoothed version of the prior model, used to start the 3-D optimization (step 2);  $m^{sol}$ : solution of the 3-D optimization.

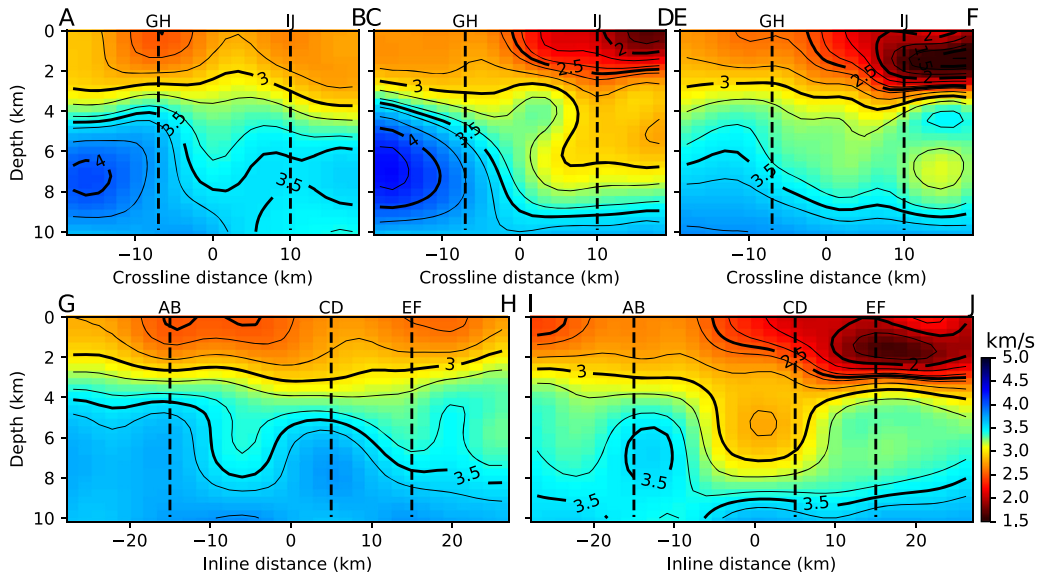


**Fig. 8.** Vertical profiles across the final 3-D  $V_S$  model obtained from SWT. The location of the slices are indicated in Figure 9.

Both models show anomalies that are in good agreement with surface geology. For example, the elliptical low velocity anomaly observed in both models in the central part of the Mauléon Basin and elongated along the WNW-ESE direction (y1 in Figs. 10, 12 and 13) *i.e.*, parallel to the strike of the main orogenic structures, corresponds to the core of a mapped

syncline. The core of this syncline is filled by Upper Cretaceous turbidites with Lower Cretaceous and Jurassic marls and limestones underneath. Conversely, the Saint-Palais anticline in the central part of the C1-C3 section is characterized by higher seismic velocities (y2 in Figs. 10 and 13). The low velocity anomaly y3 in Figures 10 and 11,

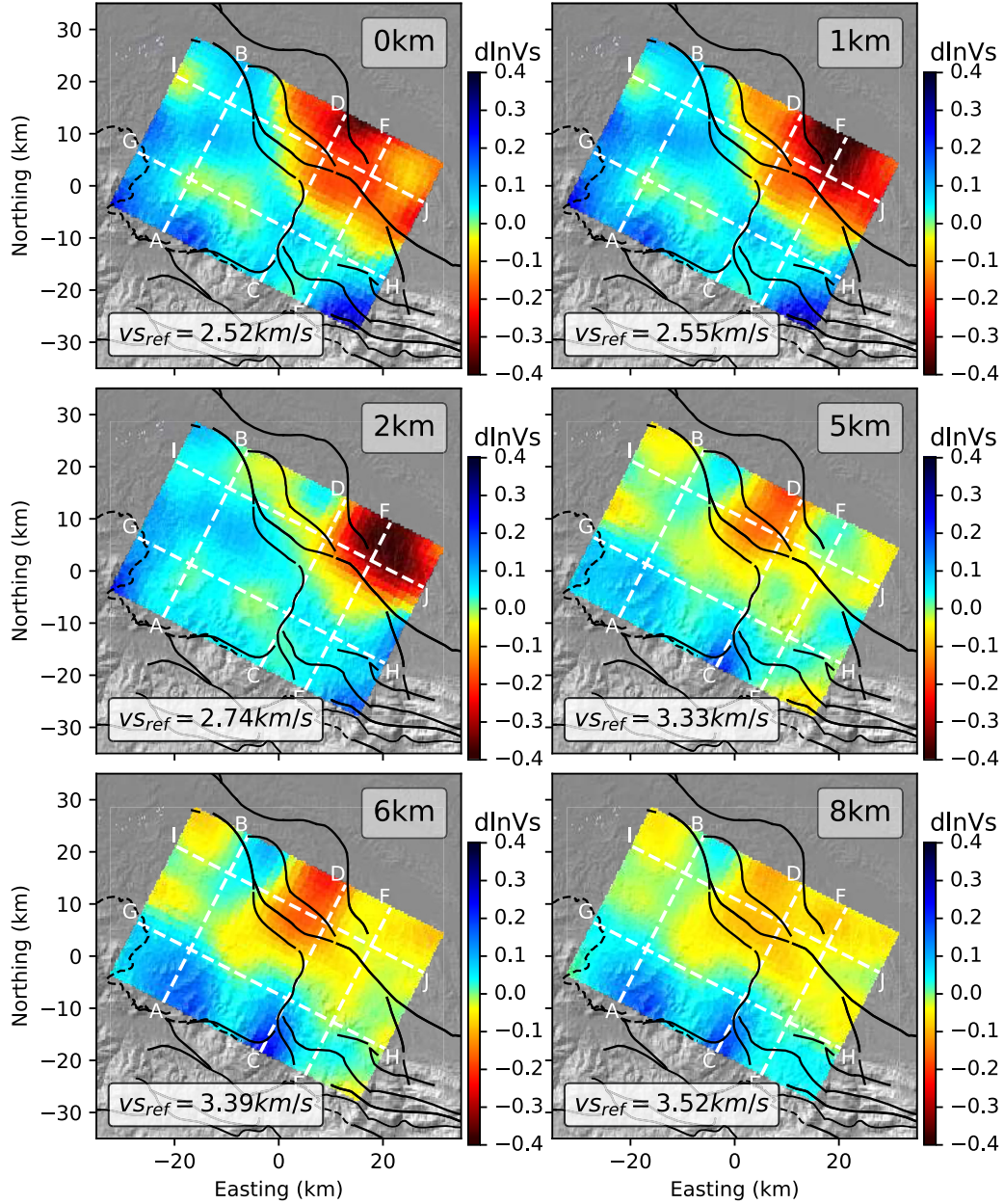


**Fig. 9.** Horizontal sections in the final 3-D  $V_S$  model obtained from SWT. The black lines indicate the main faults.

seen in both models, is related to the Cenozoic sediments accumulated in the Aquitaine Basin. On map view, the regional shape of the NPFT, which juxtaposes Mesozoic rocks onto younger sediments and makes a lateral ramp north of the Saison structure, has a clear signature at shallow depth in both models (y4 in Fig. 10). Finally, the higher velocities in the southern part of the models can be related to the metamorphic rocks of the Arbailles and Labourd Paleozoic Massifs (Fig. 10).

In Figures 14–16, we compare our tomographic models with seismic reflection profiles, surface geology and well data from some key boreholes of the Mauléon Basin (details in Supplementary Materials S1 and S2). In order to facilitate

these comparisons, we converted our models from depth to two-way travel times using

$$\text{twt}(x, z) = 2 \left[ \int_{z_{\text{topo}}}^z \frac{dy}{V_P(x, y)} + \frac{z_{\text{topo}} - z_{\text{srd}}}{V_{\text{rep}}} \right], \quad (12)$$

where  $\text{twt}(x, z)$  is the two-way travel time corresponding to depth  $z$  and position  $x$  along the profile,  $V_P$  the P-wave velocity estimated by multiplying the  $V_S$  by a  $V_P/V_S$  ratio of 1.73,  $z_{\text{srd}}$  the reference level taken at 500 m above the sea level,  $z_{\text{topo}}$  the topography level, and  $V_{\text{rep}}$  the replacement velocity chosen at 2.5 km/s. The time adjustment related to  $z_{\text{srd}}$  and  $V_{\text{rep}}$  is used to avoid propagating the irregular surface topography in the twt

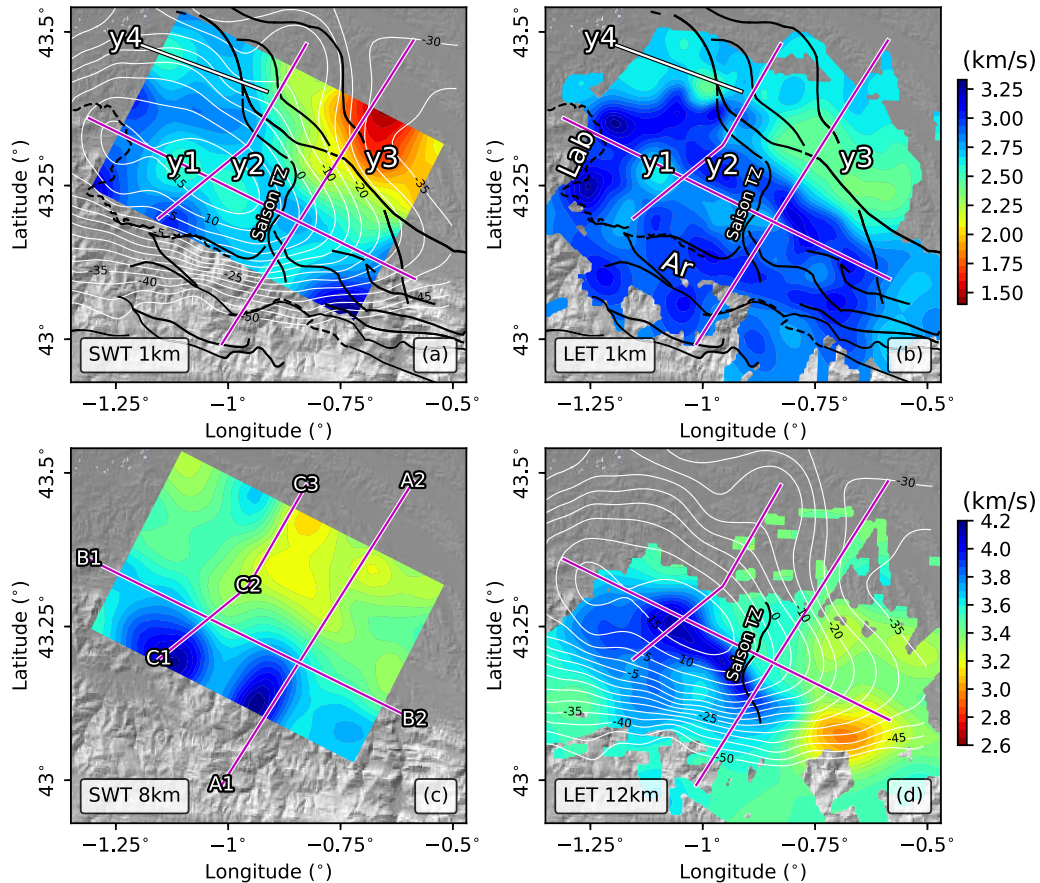


**Fig. 10.** Map views of  $V_S$  models from SWT (a,c) and LET (b,d) at several depths. The pink lines indicate the positions of sections A1-A2, B1-B2, C1-C2-C3 shown in Figures 11–16. The anomalies y1 to y4 are discussed in the text. The thick black lines correspond to main faults and the thin black dashed line corresponds to the basement-sediment interface to the south of the Mauléon Basin. The thin white lines in maps (a, d) correspond to the contour of the Bouguer anomaly in mgal from Figure 2A. Maps (a, b) and (c, d) share the same color bar. Ar: Arbailles Massif; Lab: Labour Massif; Saison TS: Saison Transverse Structure.

profile. It consists in filling the volume between the topography and the reference level by an imaginary layer of constant velocity. The values chosen for  $V_{rep}$  and  $z_{srd}$  have little impact on the resulting figures.

In the central part of the western section (Fig. 15), a velocity inversion is observed at  $\sim 2$  s TWT in the SWT model (Fig. 15A). This inversion is in good agreement with the Bellevue well, which documents Jurassic marls and limestones over the imbricated Lower Cretaceous limestones and Upper Triassic evaporites (Fig. S1). This tectonic contact probably corresponds to the Bellevue Thrust that is cropping out at the surface further north. A similar velocity inversion can be recognized in the northern part of the SWT model on the western section at 2.5 s TWT. This depth corresponds to the occurrence of the Sainte-Suzanne Thrust in the Orthez well that brings shallow high-velocity rocks (Lower Cretaceous and Jurassic carbonates) on top of younger clastics sediments (Fig. S1). Further south, a shallow and smooth vertical velocity inversion can also be observed north of the Arbailles Massif, where the nearby Ainhice well documented a duplication of the stratigraphy at depth (Lescoutre *et al.*, 2019, 2021; Saspiturry *et al.*, 2019b; Fig. S1). This structure could correspond to a thin-skin thrust at the front of the Arbailles Massif (Fig. 15).

## 5 Discussion

### 5.1 Limits of passive imaging methods

Part of the resolution discrepancy observed between SWT and LET may be explained from the different parameterization and regularization schemes used in the two types of inversions. However, because velocity anomalies tend to be smeared along the propagation directions, surface waves better constrain vertical structural variations compared to horizontal ones, whereas for body waves it is the opposite. Vertical smearing is indeed strongly expressed in the LET model, particularly at shallow depth. This may partly explain the smaller amplitudes of velocity anomalies in the upper crust in this model. The comparison of LET and SWT also reveals that whereas the shallow velocity anomalies in the two models are rather well correlated, the LET model is on average faster than the SW model. This suggests that the starting 1-D model used in the LET inversion is on average too fast, a bias that remains in the final 3-D model. This can simply be understood by the trade-off between the average velocity model and the origin time of the earthquakes. Therefore, the initial model used in LET still has a strong imprint on the final 3-D model, and it is

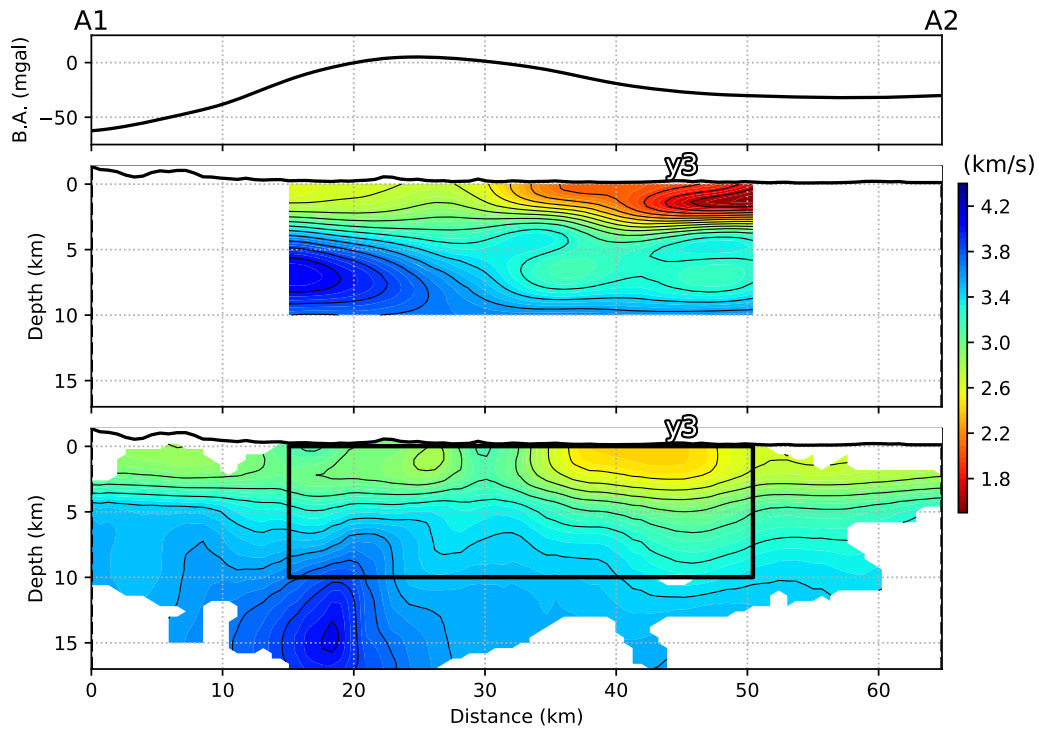


**Fig. 11.** Comparison of  $V_S$  models obtained from SWT (top) and LET (bottom) along a SW-NE transect A1-A2 crossing the Arzacq Basin (location in Fig. 10). Anomaly  $y_3$  is discussed in the text. B.A.: Bouguer Anomaly extracted along the profile from the gravity map of Figure 2A.

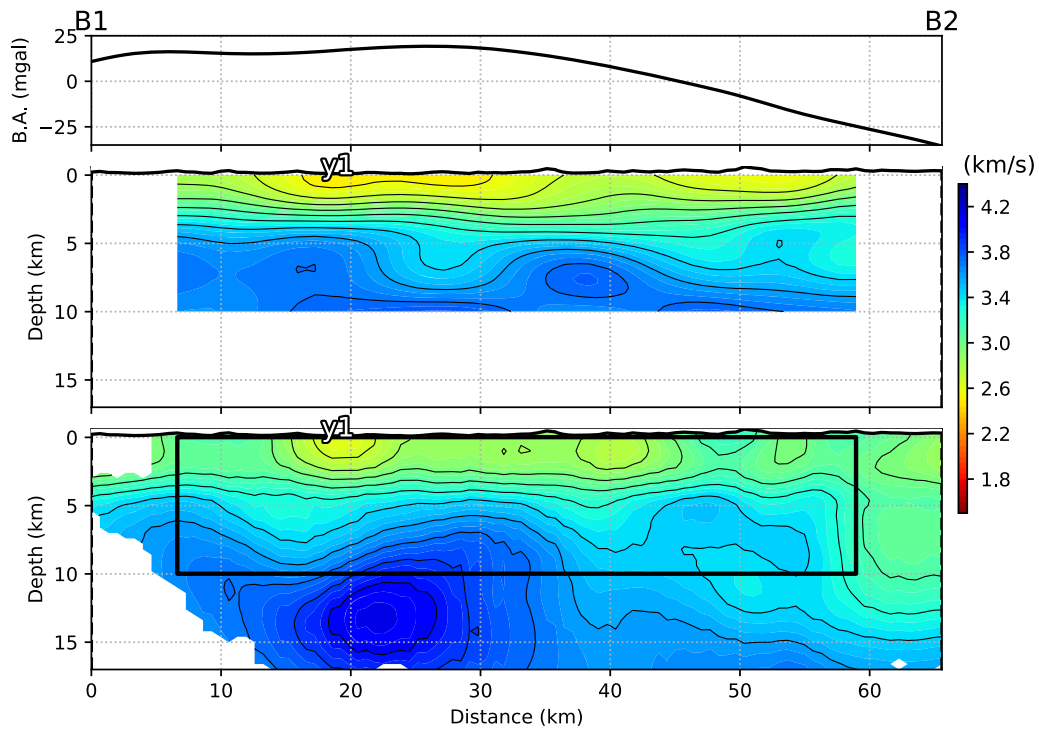


**Fig. 12.** Comparison of  $V_S$  models obtained from SWT (top) and LET (bottom) along a WNW-ESE transect B1-B2 crossing the Mauléon Basin (location in Fig. 10). Anomaly  $y_1$  is discussed in the text. B.A.: Bouguer Anomaly extracted along the profile from the gravity map of Figure 2A.

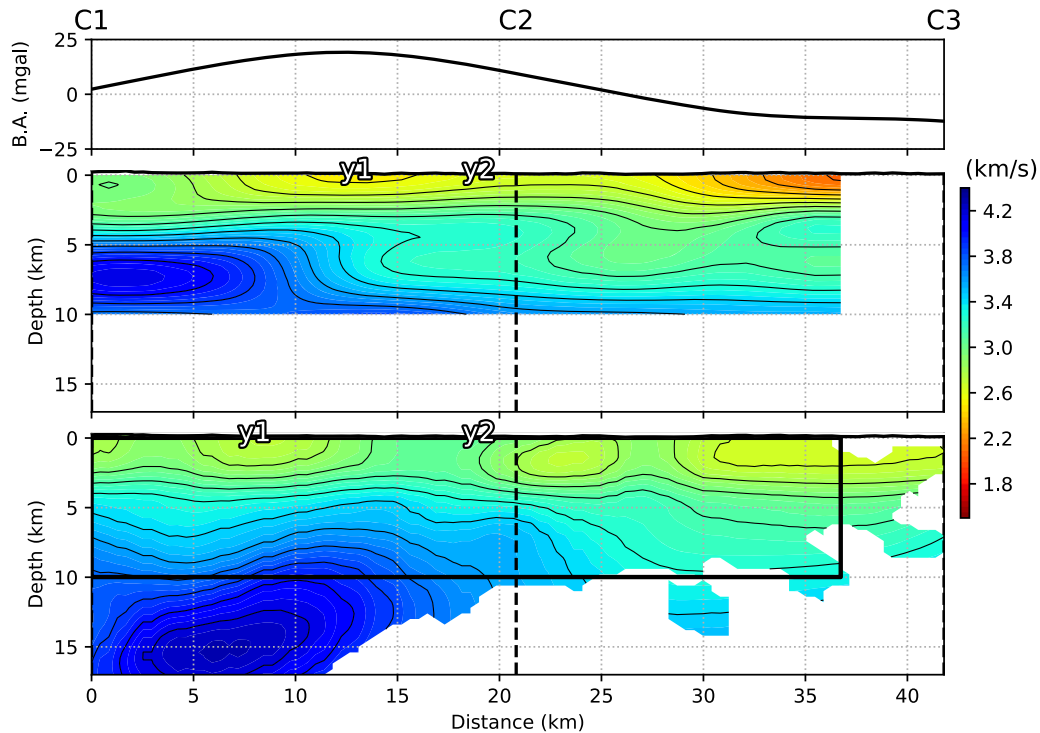


**Fig. 13.** Comparison of  $V_S$  models obtained from SWT (top) and LET (bottom) along a SW-NE transect C1-C2-C3 crossing the Mauléon Basin (location in Fig. 10). Anomalies  $y_1$ ,  $y_2$  are discussed in the text. B.A.: Bouguer Anomaly extracted along the profile from the gravity map of Figure 2A.

thus crucial to build this model very carefully, using all the *a priori* information that is available. SWT could provide such key constraints on absolute velocities, in particular at shallow levels.

Other important differences come from the intrinsic limitations of both approaches. In LET, the resolution is controlled by ray coverage, and thus by the distribution of earthquakes. In the Western Pyrenees, the seismicity is concentrated inside a narrow band that approximately follows the limit between the Axial Zone and the North Pyrenean Zone, with hypocentral depths rarely exceeding 20 km (Souriau and Pauchet, 1998b; Chevrot *et al.*, 2011). Owing to the distribution of earthquakes, the resolution is thus limited to the top 15 km, but it degrades notably beneath the Arzacq Basin at depths below 10 km. In contrast, the main limitation of SWT comes from the amplitude and distribution of noise sources, the geometry of the array, and the sensor types. In this study, we exploited surface waves excited by energetic oceanic sources at periods from 2 to 9 s (microseismic band). At longer period, the sensitivities of geophones and short period sensors become very low, and the records are dominated by instrumental noise. Therefore, at periods longer than ~6 s only the broadband sensors can be exploited. In addition, the wavelengths of Rayleigh waves at these periods are larger than 20 km *i.e.*, of the order of the size of the region that we want to image. This may explain the degradation of the lateral resolution in the deeper part of the model, especially beneath the NW-SE Mauléon transect shown in Figure 12. On the other hand, at shorter period the station spacing ( $\geq 1$  km) becomes too coarse to sample the wavefield with at least 2 samples per

wavelength, and cycle skipping issues appear. For these reasons, the resolution is more uniform in the SWT model but limited to the top 10 km of the crust.

In any case, the similarity of LET and SWT models, in addition to the different but complementary sensitivity of body and surface waves to shallow structures, suggest that joint inversions would be a natural way to further improve the resolution and robustness of crustal tomographic models. Because these inverse problems are still solved separately with different model parameterization and regularization schemes, this will require developing a new generation of inversion codes.

## 5.2 Geological interpretations and integration into a 3-D structural model

We now attempt to build a coherent 3-D model of the Mauléon Basin. We base our interpretation mostly on the shape of the velocity anomalies observed in the new tomographic models and how these anomalies agree or not with the available geological information, gravity data and seismic profiles, keeping in mind the strengths and weaknesses of each approach discussed above. As already pointed out in the previous section, the velocity inversions can be associated with major thrusts (see Sect. 4; Fig. 15). The inversion seen on the eastern section (Fig. 14) can thus be interpreted as the southward continuation of the south-dipping NPFT beneath the bottom of the Les-Cassières-2 borehole (Fig. S2). The western profile is located to the west of the Saison structure (Fig. 2A), where the positive Bouguer gravity anomaly

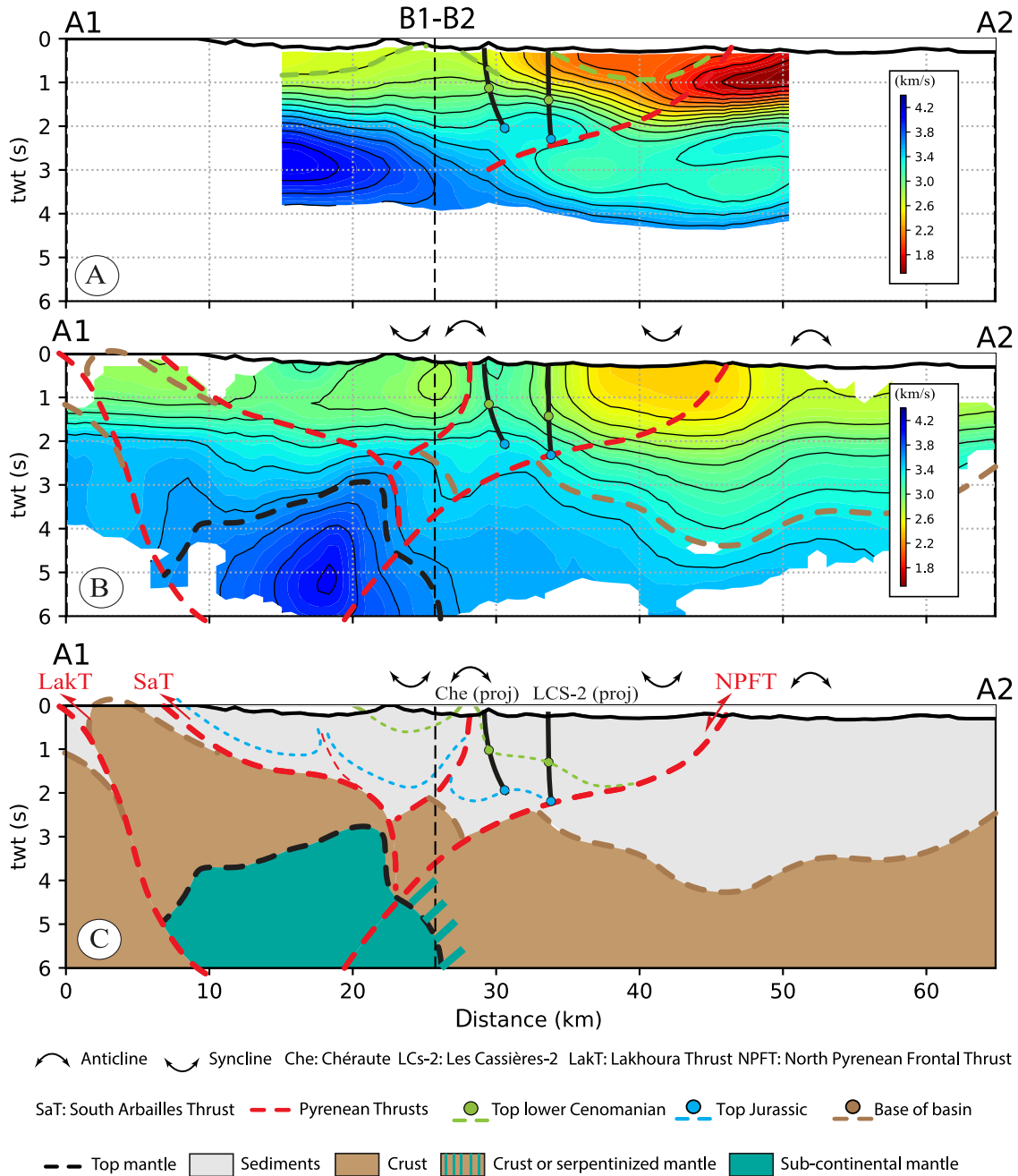


**Fig. 14.** SW-NE profile in the eastern Mauléon Basin showing the interpretation of the SWT (A) and LET (B) models. The final geological interpretation (C) is based on these models, the surface geology and boreholes. Location of axial traces of major anticlines and synclines are based on the geological map. The surface wave model successfully images the first-order basin architecture at shallow depth (syncline/anticline, faults) whereas the local earthquake tomography model provides information about the basement-sediment interface and the geometry of the high velocity body at depth.

interpreted as related to a shallow body of subcontinental mantle has been imaged by Wang *et al.* (2016). This piece of mantle is located in the hanging-wall of the Sainte-Suzanne Thrust (Fig. 15). East of the Saison structure, the high velocity mantle body is laterally shifted to the south and replaced by lower velocity rocks in the hanging wall of the steeper NPFT. These rocks might correspond to middle/lower crustal

(metamorphic) rocks, serpentinized mantle or sedimentary rocks. The geometry of the iso-velocity lines at depth, in both the eastern and western NS sections, suggests that the high-velocity rocks ( $V_S > 3.8$  km/s) get shallower towards the north underneath the Mauléon Basin, and thus that upper crustal rocks thin at the expense of deeper lithospheric rocks. Note that similar relationships between basement velocities and crustal

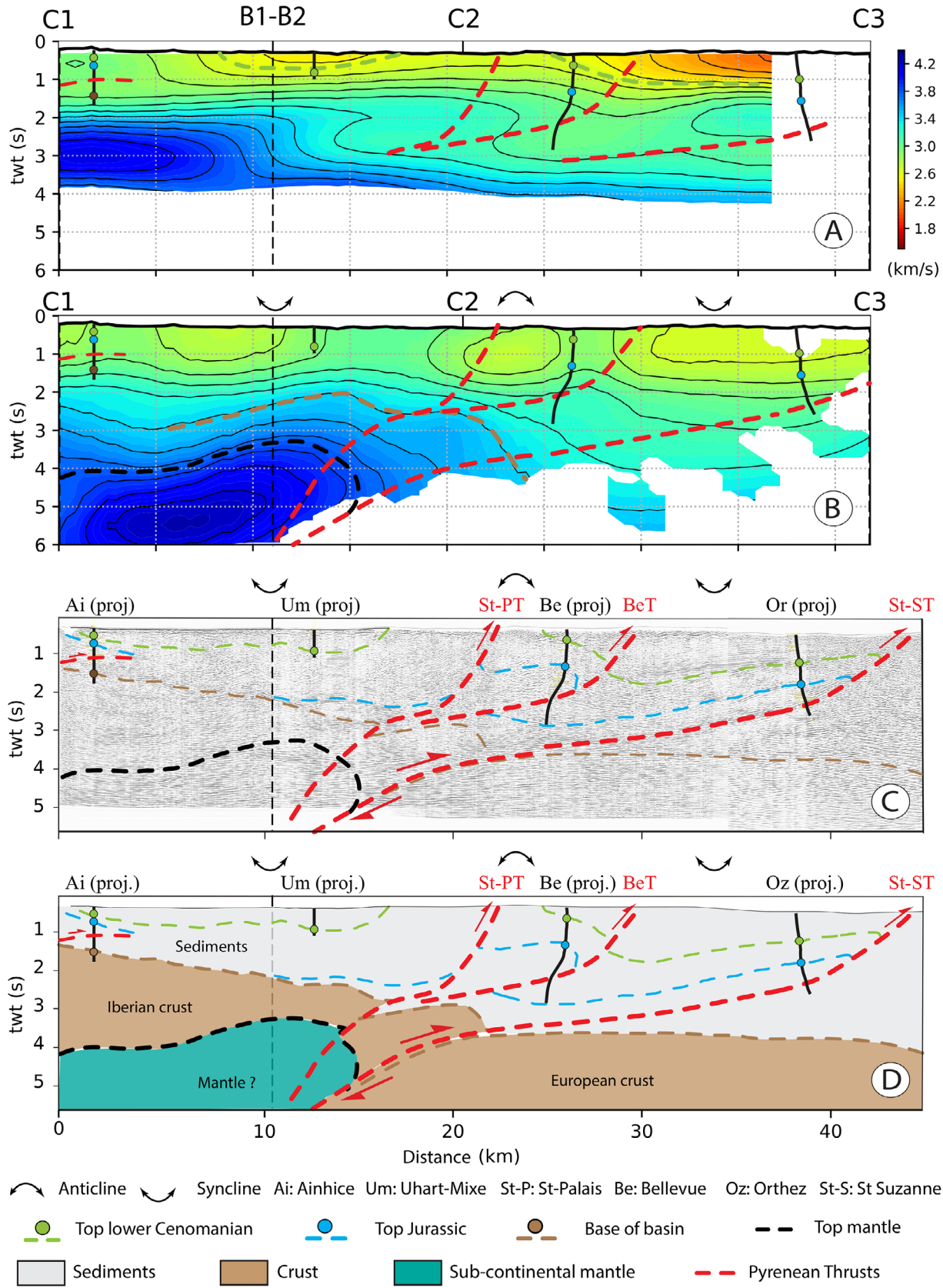


**Fig. 15.** SW-NE profile in the western Mauléon Basin showing the interpretation of the SWT model (A), the LET model (B), the NS seismic reflection profile (C) and the final geological interpretation (D). Note the difference in the basin architecture and the basement geometry in comparison to the eastern Mauléon section of [Figure 14](#).

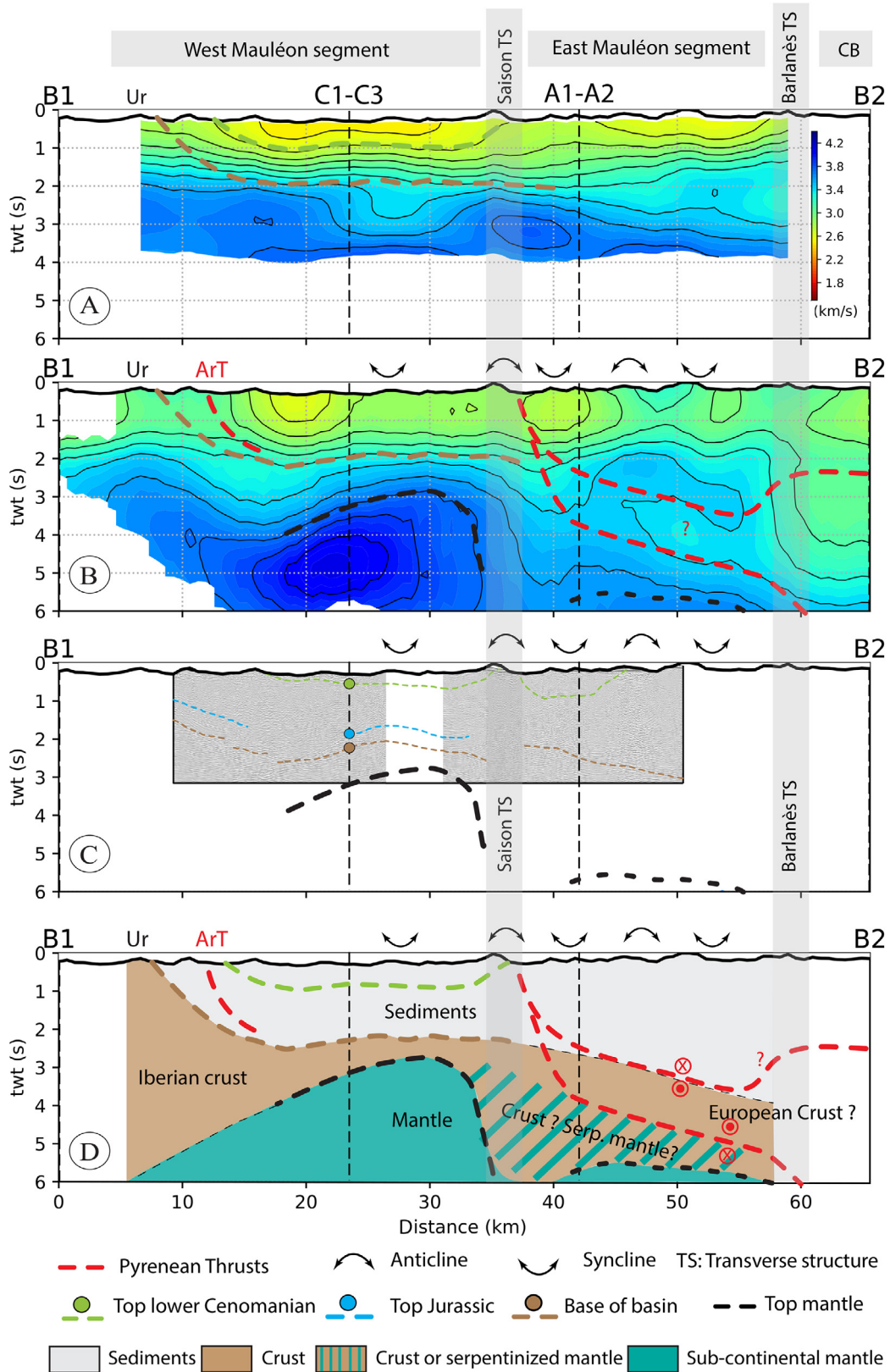


**Fig. 16.** WNW-ESE profile in the Mauléon Basin showing the interpretation of the SWT model (A), the LET model (B), the seismic reflection profile (C) and the geological interpretation (D). Note the very high velocity body in the western Mauléon segment of the section, contrasting with the complex velocity inversion in the eastern Mauléon segment and the low velocity body in the Chaînons Béarnais segment, highlighting the importance of the Saison and Barlanès TS for the along-strike orogenic architecture of the study area. Correlating this section with the N-S sections further reveal that the intermediate unit bracketed by two velocity inversions in the eastern Mauléon segment should be the tip of the European Unit *i.e.*, the European indenter between two thrusts.

tapering were reported from offshore Ocean-Continent transitions such as the Iberian (Dean *et al.*, 2000) or the Newfoundland (Lau *et al.*, 2006) margins. This interpretation is in line with previous models from the Mauléon Basin involving north-dipping detachment faults exhuming granulite and subcontinental mantle rocks (Jammes *et al.*, 2009; Masini *et al.*, 2014; Gómez-Romeu *et al.*, 2019; Saspiturry *et al.*, 2019b; Lescoutre *et al.*, 2019).

In the along-strike section (Fig. 16), the 3.2–3.6 km/s iso-velocity lines become shallower at the western edge of the LET profile where the basement rocks of the Labourd Massif are cropping out (Fig. 2B). The trend of these iso-velocity lines indicate the geometry of the top basement at depth. At the eastern edge of the E-W section, the high velocities at shallow depth are in good agreement with the nappe-stack of the Chaînons Béarnais that consists of mixed sedimentary cover (including metamorphosed carbonates) and basement rocks (including serpentinized mantle bodies) (Labaume and Teixell, 2020). At depth, in the central part of the model, a steep velocity contrast between high velocities to the west and lower velocities to the east can be observed on the LET model (Fig. 16). In the easternmost part of the E-W profile, a similar observation can be made with an abrupt change towards lower velocities to the east. These steep velocity gradients correspond to the location at depth of the Saison and Barlanès transverse structures mapped at the surface (Fig. 2B). Therefore, these structures are segmenting the Mauléon Basin and the Chaînons Béarnais in a roughly orogen-perpendicular direction. As seismic velocities are to first-order positively correlated to densities, this observation is consistent with the eastward attenuation of the positive gravity anomaly attributed to shallow mantle rocks across the Saison and Barlanès structures (Figs. 2A and 12). The exact nature of the basement rocks and the depth of the Moho on both sides of the Saison structure remain poorly constrained. However, as stated above, the tomographic model of Wang *et al.* (2016) suggests the presence of subcontinental mantle at shallow depth (10 km) below the western Mauléon segment. Because the LET model shows relatively lower velocities from the west to the east of the Saison structure, and the gravity anomaly shows a similar transition (Fig. 12), the basement of the eastern Mauléon segment is most likely made of less dense material more altered/serpentinized (*e.g.*, mantle rocks or mafic/metamorphic lower crust). This interpretation is in good agreement with previous structural models that interpreted the Saison structure as a crustal transfer zone active during the Pyrenean orogeny (Masini *et al.*, 2014; Lescoutre and Manatschal, 2020; Saspiturry, 2019). The Saison and Barlanès structures accommodated deformation between the western Mauléon segment, where the hyperextended rift domain together with the subcontinental mantle rocks have been transported in the hanging wall of a north-vergent thrust, and the Chaînons Béarnais segment, where most of this hyperextended domain has been underthrust beneath the European crust (Fig. 17). This distributed deformation also suggests a change in the structural level of indentation during the orogeny. While the European crust anomalously indented the Iberian mantle at an early stage of convergence in the west leading to its shallow sampling (*i.e.*, thick-skinned style, see Lescoutre and Manatschal, 2020), it is likely that the indentation rather used

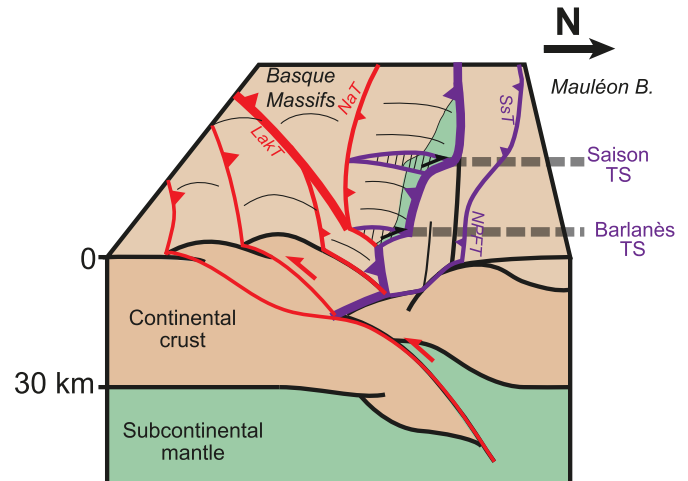


**Fig. 17.** Schematic 3-D block diagram showing the segmentation of the crustal architecture in the Mauléon Basin as inferred from this study. Note the sampling of hyper-extended crust and mantle towards the west across the Saison and Barlanès TS. Basin sediments are not represented to highlight the basement structures. Annotations correspond to Figure 2. Figure modified after Lescoutre and Manatschal (2020).

the basement-sediment interface in the east (Fig. 17). This scenario explains the apparent increase of thin-skinned shortening eastward, because of a significant accommodation of shortening within the basement in the west. Note that these complex 3-D structures are restricted to the hanging-wall of the north-dipping “slab” previously imaged by Wang *et al.* (2016) that should be consistently made of the Iberian basement formerly located in the southern border of the basin.

## 6 Conclusion

Our study demonstrates that, using dense large-N deployments, it is possible to obtain finely resolved images of fold and thrust belts from the exploitation of surface and body waves with passive imaging approaches. Obviously, the level of details in our tomographic images is not on par with a typical seismic reflection survey and resolving the different sedimentary horizons inside a sedimentary basin is clearly beyond the reach of surface wave tomography. Nevertheless, our study provides robust first-order constraints on the deep architecture of the Mauléon and Arzacq Basins, where previous controlled source seismic reflection studies actually gave rather poor results, and for a fraction of the cost of such acquisitions. In particular, our tomographic models confirm the presence of orogen-perpendicular structures in the study area that controlled the along-strike change in the orogenic basement structure and composition. They also control the local preservation of hyper-extended rifted crust and mantle at shallow depth going along the gravimetric anomaly. We are thus convinced that passive imaging represents a valuable source of information that should be considered in the future, especially in environments where controlled source acquisitions are challenging or are impeded by legislation.

## Supplementary Material

**Figure S1.** Wells data from the western segment covering the Mauléon Basin in the south (Ainhice, Uhart-Mixe, Bellevue wells) and the Aquitaine Basin (Amou well). After [Saspiturry \*et al.\* \(2019a, 2020b\)](#).

**Figure S2.** Wells data from the eastern segment covering the eastern Mauléon Basin (Chéraute and Les Cassières-2 wells). After [Saspiturry \*et al.\* \(2019a, 2020b\)](#).

**Figure S3.** Checkerboard tests.

**Files S1–S2.** Numerical Models of the Paper.

The Supplementary Material is available at <http://www.bsgf.fr/10.1051/bsgf/2021039/olm>.

**Acknowledgement.** This work was supported by OROGEN, a tripartite research project between the CNRS, TOTAL and BRGM, and by the ANR AAPG program (project CLEARVIEW, ANR-17-CE23-0022). AV received funding from the Spanish government through the “Severo Ochoa Centre of Excellence” accreditation (CEX2019-000928-S). We thank associate editor David Pedreira, as well as Josep Antón Muñoz and an anonymous reviewer for their constructive comments.

## References

- Aki K, Richards PG. 2002. Quantitative seismology. University Science Books.
- Angrand P, Ford M, Watts AB. 2018. Lateral variations in foreland flexure of a rifted continental margin: The Aquitaine Basin (SW France). *Tectonics* 37(2): 430–449.
- Asti R, Lagabrielle Y, Fourcade S, Corre B, Monié P. 2019. How do continents deform during mantle exhumation? insights from the Northern Iberia inverted paleopassive margin, Western Pyrenees (France). *Tectonics* 38(5): 1666–1693.
- Benz HM, Chouet BA, Dawson PB, Lahr JC, Page RA, Hole JA. 1996. Three dimensional P- and S-wave velocity structure of Redoubt volcano, Alaska. *Journal of Geophysical Research* 101 (B4): 8111–8128.
- Bodet L, van Wijk K, Bitri A, Abraham O, Côte P, Grandjean G, *et al.* 2005. Surface-wave inversion limitations from laser-doppler physical modeling. *Journal of Environmental, Engineering Geophysics* 10(2): 151–162.
- Boillot G, Capdevilla R, Hennequin-Marchand I, Lamboy M, Lepretre JP. 1973. La zone nord-pyrénéenne, ses prolongements sur la marge continentale nord-espagnole et sa signification structurale. *Comptes rendus de l'Académie des sciences (Paris)* 227: 2629–2632.
- Boissonnas J, Destombes J, Heddebaut C, Le Pochat G, Lorisignol S, Roger P, *et al.* 1974. Feuille de iholdy (1027). Carte géologique de la France, scale 1/50 000. Bureau de Recherche Géologique et Minières.
- Brocher TM. 2005. Empirical relations between elastic wavespeeds and density in the earth's crust. *Bulletin of the seismological Society of America* 95(6): 2081–2092.
- Canérot J. 2017. The pull apart-type tardiets-Mauléon Basin: A key to understand the formation of the Pyrenees. *Bull. Soc. géol. Fr.* 188(6): 35.
- Canérot J, Majesté-Menjoulas C, Ternet Y. 1999. Le cadre stratigraphique et géodynamique des altérites et des bauxites sur la marge ibérique des pyrénées occidentales (France). *Comptes Rendus de l'Académie des Sciences – Series IIA – Earth and Planetary Science* 328(7): 451–456.
- Casas A, Kearey P, Rivero L, Adam CR. 1997. Gravity anomaly map of the Pyrenean region and a comparison of the deep geological structure of the Western and Eastern Pyrenees. *Earth and Planetary Science Letters* 150(1-2): 65–78.
- Chevrot S, Sylvander M, Delouis B. 2011. A preliminary catalogue of moment tensors for the Pyrenees. *Tectonophysics* 510: 239–251.
- Chevrot S, Villaseñor A, Sylvander M, The Pyrope Team. 2014. High resolution imaging of the Pyrenees and Massif Central from the data of the PYROPE and IBERARRAY portable array deployments. *J. Geophys. Res.* 119(8): 6399–6420. <https://doi.org/10.1002/2014JB010953>.
- Chevrot S, Sylvander M, Diaz J, Ruiz M, Paul A, The PYROPE Working Group. 2015. The Pyrenean architecture as revealed by teleseismic P-to-S converted waves recorded along two dense transects. *Geophys. J. Int.* 200: 1096–1107.
- Chevrot S, Sylvander M, Diaz J, Martin R, Mouthereau F, Manatschal G, *et al.* 2018. The non-cylindrical crustal architecture of the Pyrenees. *Scientific Reports* 8(1): 9591.
- Corre B, Lagabrielle Y, Labaume P, Fourcade S, Clerc C, Ballèvre M. 2016. Deformation associated with mantle exhumation in a distal, hot passive margin environment: New constraints from the Sarailié Massif (Châinons Béarnais, North-Pyrenean Zone). *Comptes Rendus Geoscience* 348(3-4): 279–289.
- Curnelle R. 1983. Évolution structuro-sédimentaire du trias et de l'infra-lias d'Aquitaine. *Bulletin des Centres de recherches exploration-production Elf-Aquitaine* 7(1): 69–99.
- Daignières M, Séguret M, Specht M, ECORS Team. 1994. The Arzacq-Mauléon-Western Pyrenees ECORS Deep Seismic Profile. In: Mascle A, ed. *Hydrocarbon and Petroleum Geology of France*, vol. 4, Eur. Assoc. Pet. Geosci. Spec. Publ., pp.199–208. Academic, USA: Springer-Verlag.
- Dean S, Minshull T, Whitmarsh R, Loudon K. 2000. Deep structure of the ocean-continent transition in the Southern Iberia abyssal plain from seismic refraction profiles: The iam-9 transect at 40° N. *Journal of Geophysical Research: Solid Earth* 105(B3): 5859–5885.
- Debroas EJ, Canérot J, Bilotte M. 2010. Les brèches d'Urdach, témoins de l'exhumation du manteau pyrénéen dans un escarpement de faille vraconnien-cénomaniens inférieur (Zone nord-pyrénéenne, Pyrénées-Atlantiques, France). *Géologie de la France* 2: 53–63.
- Dorman J, Ewing M. 1962. Numerical inversion of seismic surface wave dispersion data and crust-mantle structure in the New York-Pennsylvania area. *Journal of Geophysical Research* 67(13): 5227–5241.
- Ducoux M, Masini E, Tugend J, Gómez-Romeu J, Calassou S. 2021. Basement-decoupled hyper-extension rifting: The tectono-stratigraphic record of the salt-rich pyrenean necking zone (Arzacq Basin, SW France). *GSA Bulletin*.
- Dumont T, Replumaz A, Rouméjon S, Briais A, Rigo A, Bouillin J-P. 2015. Microseismicity of the béarn range: Reactivation of inversion and collision structures at the northern edge of the Iberian plate. *Tectonics* 34(5): 934–950.
- Fang H, Yao H, Zhang H, Huang Y-C, van der Hilst RD. 2015. Direct inversion of surface wave dispersion for three-dimensional shallow crustal structure based on ray tracing: methodology and application. *Geophysical Journal International* 201(3): 1251–1263.
- Fortané A, Duée G, Lagabrielle Y, Coutelle A. 1986. Lherzolites and the Western “Châinons Béarnais”? (French Pyrenees): Structural and paleogeographical pattern. *Tectonophysics* 129(1-4): 81–98.
- Gassenmeier M, Sens-Schönfelder C, Delatre M, Korn M. 2014. Monitoring of environmental influences on seismic velocity at the geological storage site for CO<sub>2</sub> in Ketzin (Germany) with ambient seismic noise. *Geophysical Journal International* 200(1): 524–533.

- Gilbert F, Backus GE. 1966. Propagation matrices in elastic wave and vibration problems. *Geophysics* 31(2): 326–332. GeoScienceWorld.
- Gómez-Romeu J, Masini E, Tugend J, Ducoux M, Kuszniir N. 2019. Role of rift structural inheritance in orogeny highlighted by the Western Pyrenees case-study. *Tectonophysics* 766: 131–150.
- Gottis M. 1972. Construction d'un modèle géodynamique pyrénéen. *Comptes Rendus Académie des Sciences* 275.
- Grandjean G. 1994. Etude des structures crustales dans une portion de chaîne et de leur relation avec les bassins sédimentaires. Application aux Pyrénées occidentales. *Bull. Cent. Rech. Explor. Prod. Elf Aquitaine* 18(2): 391–420.
- Hansen PC, O'Leary DP. 1993. The use of the l-curve in the regularization of discrete ill-posed problems. *SIAM Journal on Scientific Computing* 14(6): 1487–1503.
- Haskell NA. 1953. The dispersion of surface waves on multilayered media. *Bulletin of the Seismological Society of America* 43(1): 17–34.
- Herrmann RB. 2013. Computer programs in seismology: An evolving tool for instruction and research. *Seismological Research Letters* 84 (6): 1081–1088.
- Issautier B, Saspiturry N, Serrano O. 2020. Role of structural inheritance and salt tectonics in the formation of pseudosymmetric continental rifts on the European margin of the hyperextended Mauléon Basin (Early Cretaceous Arzacq and Tartas Basins). *Marine and Petroleum Geology* 118: 104395.
- Jammes S, Manatschal G, Lavier L, Masini E. 2009. Tectonosedimentary evolution related to extreme crustal thinning ahead of a propagating ocean: Example of the Western Pyrenees. *Tectonics* 28: TC4012. <https://doi.org/10.1029/2008TC002406>.
- Jammes S, Tiberi C, Manatschal G. 2010. 3-D architecture of a complex transcurrent rift system: The example of the Bay of Biscay-Western Pyrenees. *Tectonophysics* 489(1-4): 210–226.
- Jia Z, Clayton RW. 2021. Determination of near surface shear-wave velocities in the Central Los Angeles Basin with dense arrays.
- Knopoff L. 1964. A matrix method for elastic wave problems. *Bulletin of the Seismological Society of America* 54(1): 431–438.
- Labaume P, Teixell A. 2020. Evolution of salt structures of the Pyrenean Rift (Chaînons Béarnais, France): From hyper-extension to tectonic inversion. *Tectonophysics* 785: 228451.
- Lagabrielle Y, Labaume P, de Saint Blanquat M. 2010. Mantle exhumation, crustal denudation, and gravity tectonics during Cretaceous rifting in the Pyrenean realm (SW Europe): Insights from the geological setting of the lherzolite bodies. *Tectonics* 29(4).
- Lagabrielle Y, Asti R, Fourcade S, Corre B, Poujol M, Uzel J, *et al.* 2019. Mantle exhumation at magma-poor passive continental margins. Part I. 3-D architecture and metasomatic evolution of a fossil exhumed mantle domain (Urdach lherzolite, North-Western Pyrenees, France). *BSGF–Earth Sciences Bulletin* 190: 8.
- Lau KH, Loudon KE, Funck T, Tucholke BE, Holbrook WS, Hopper JR, *et al.* 2006. Crustal structure across the grand banks-newfoundland basin continental margin-i. Results from a seismic refraction profile. *Geophysical Journal International* 167(1): 127–156.
- Lehujeur M, Chevrot S. 2020. Eikonal tomography using coherent surface waves extracted from ambient noise by iterative matched filtering-application to the large-n Maupasacq array. *Journal of Geophysical Research: Solid Earth* 125(6).
- Lehujeur M, Vergne J, Schmittbuhl J, Zigone D, Le Chenadec A, Team ECORS. 2018. Reservoir imaging using ambient noise correlation from a dense seismic network. *Journal of Geophysical Research: Solid Earth* 123(8): 6671–6686.
- Leleu S, Hartley AJ, van Oosterhout C, Kennan L, Ruckwied K, Gerdes K. 2016. Structural, stratigraphic and sedimentological characterisation of a wide rift system: The triassic rift system of the central atlantic domain. *Earth-Science Reviews* 158: 89–124.
- Lescoutre R. 2019. Formation et réactivation du système de rift pyrénéo-cantabrique : héritage, segmentation et évolution thermique. PhD Thesis, Strasbourg.
- Lescoutre R, Manatschal G. 2020. Role of rift-inheritance and segmentation for orogenic evolution: Example from the Pyrenean-Cantabrian system. *BSGF–Earth Sciences Bulletin* 191: 18.
- Lescoutre R, Tugend J, Brune S, Masini E, Manatschal G. 2019. Thermal evolution of asymmetric hyperextended magma-poor rift systems: Results from numerical modeling and Pyrenean field observations. *Geochemistry, Geophysics, Geosystems* 20(10): 4567–4587.
- Lescoutre R, Manatschal G, Muñoz JA. 2021. Nature, origin and evolution of the pyrenean-cantabrian junction. *Tectonics* n/a(n/a): e2020TC006134.
- Lin FC, Moschetti MP, Ritzwoller MH. 2008. Surface wave tomography of the Western United States from ambient seismic noise: Rayleigh and Love wave phase velocity maps. *Geophysical Journal International* 173(1): 281–298.
- Lomax A, Snieder R. 1994. Finding sets of acceptable solutions with a genetic algorithm with application to surface wave group dispersion in Europe. *Geophysical Research Letters* 21(24): 2617–2620. [\\_eprint: https://agupubs.onlinelibrary.wiley.com/doi/pdf/10.1029/94GL02635](https://agupubs.onlinelibrary.wiley.com/doi/pdf/10.1029/94GL02635).
- Lu Y, Stehly L, Paul A. 2018. High-resolution surface wave tomography of the European crust and uppermost mantle from ambient seismic noise. *Geophysical Journal International* 214(2): 1136–1150. Oxford Academic.
- Macchiavelli C, Vergés J, Schettino A, Fernández M, Turco E, Casciello E, *et al.* 2017. A new southern north atlantic isochron map: Insights into the drift of the iberian plate since the Late Cretaceous. *Journal of Geophysical Research: Solid Earth* 122 (12): 9603–9626.
- Macquet M, Paul A, Pedersen HA, Villaseñor A, Chevrot S, Sylvander M, *et al.* 2014. Ambient noise tomography of the Pyrenees and the surrounding regions: Inversion for a 3-D  $V_S$  model in the presence of a very heterogeneous crust. *Geophysical Journal International* 199(1): 402–415.
- Maraschini M, Foti S. 2010. A Monte Carlo multimodal inversion of surface waves. *Geophysical Journal International* 182(3): 1557–1566.
- Masini E, Manatschal G, Tugend J, Mohn G, Flament JM. 2014. The tectono-sedimentary evolution of a hyper-extended rift basin: The example of the Arzacq-Mauléon Rift System (Western Pyrenees, France). *Int. J. Earth Sci.* 103: 1569–1596.
- Montagner J, Tanimoto T. 1990. Global anisotropy in the upper mantle inferred from the regionalization of phase velocities. *J. Geophys. Res.* 95: 4797–4819.
- Mordret A, Shapiro N, Singh S, Roux P, Barkved O. 2013. Helmholtz tomography of ambient noise surface wave data to estimate Scholte wave phase velocity at Valhall Life of the field. *Geophysics* 78(2): WA99–WA109.
- Mordret A, Landès M, Shapiro NM, Singh SC, Roux P. 2014. Ambient noise surface wave tomography to determine the shallow shear velocity structure at Valhall: Depth inversion with a Neighbourhood Algorithm. *Geophysical Journal International* 198(3): 1514–1525. Oxford Academic.
- Mouthereau F, Filleaudeau P-Y, Vacherat A, Pik R, Lacombe O, Fellin MG, *et al.* 2014. Placing limits to shortening evolution in the Pyrenees: Role of margin architecture and implications for the iberia/europe convergence. *Tectonics* 33(12): 2283–2314.

- Olivet JL. 1996. La cinématique de la plaque ibérique. *Bull. Cent. Rech. Explor. Prod. Elf Aquitaine* 20(1): 131–195.
- Pedreira D, Pulgar JA, Gallart J, Torné M. 2007. Three-dimensional gravity and magnetic modeling of crustal indentation and wedging in the western Pyrenees-Cantabrian Mountains. *Journal of Geophysical Research* 112(B12).
- Planès T, Obermann A, Antunes V, Lupi M. 2019. Ambient-noise tomography of the Greater Geneva Basin in a geothermal exploration context. *Geophysical Journal International* 220(1): 370–383.
- Podvin P, Lecomte I. 1991. Finite difference computation of travel times in very contrasted velocity models: A massively parallel approach and its associated tools. *Geophysical Journal International* 105: 271–284.
- Polychronopoulou K, Lois A, Martakis N, Chevrot S, Sylvander M, Diaz J, *et al.* 2018. Broadband, short-period or geophone nodes? Quality assessment of passive seismic signals acquired during the Maupasacq experiment. *First Break* 36(4): 71–76.
- Puigdefàbregas C, Souquet P. 1986. Tecto-sedimentary cycles and depositional sequences of the Mesozoic and Tertiary from the Pyrenees. *Tectonophysics* 129(1-4): 173–203.
- Rat P. 1988. The Basque-Cantabrian Basin between the Iberian and European plates: some facts but still many problems. *Revista de la Sociedad geológica de España* 1(4): 327–348.
- Razin P. 1989. Évolution tecto-sédimentaire alpine des Pyrénées basques à l'ouest de la transformante de Pamplona, Province du Labourd. PhD Thesis, Bordeaux 3.
- Richard P. 1986. Structure et évolution alpine des massifs paléozoïques du Labourd (Pays Basque Français). Éditions du Bureau de recherches géologiques et minières.
- Rosenbaum G, Lister GS, Duboz C. 2002. Relative motions of Africa, Iberia and Europe during Alpine orogeny. *Tectonophysics* 359(1-2): 117–129.
- Sambridge M. 1999. Geophysical inversion with a neighbourhood algorithm-I. Searching a parameter space. *Geophysical Journal International* 138(2): 479–494. Oxford Academic.
- Saspiturry N. 2019. Évolution sédimentaire, structurale et thermique d'un rift hyper-aminci : de l'héritage post-hercynien à l'inversion alpine : exemple du bassin de Mauléon (Pyrénées). PhD Thesis, Bordeaux 3.
- Saspiturry N, Cochelin B, Razin P, Leleu S, Lemirre B, Bouscary C, *et al.* 2019a. Tectono-sedimentary evolution of a rift system controlled by Permian post-orogenic extension and metamorphic core complex formation (Bidarray Basin and Ursuya dome, Western Pyrenees). *Tectonophysics* 768: 228180.
- Saspiturry N, Razin P, Baudin T, Serrano O, Issautier B, Lasseur E, *et al.* 2019b. Symmetry vs. asymmetry of a hyper-thinned rift: Example of the Mauléon Basin (Western Pyrenees, France). *Marine and Petroleum Geology* 104: 86–105.
- Saspiturry N, Allanic C, Razin P, Issautier B, Baudin T, Lasseur E, *et al.* 2020a. Closure of a hyperextended system in an orogenic lithospheric pop-up, Western Pyrenees: The role of mantle buttressing and rift structural inheritance. *Terra Nova* 32(4): 253–260.
- Saspiturry N, Lahfid A, Baudin T, Guillou-Frottier L, Razin P, Issautier B, *et al.* 2020b. Paleogeothermal gradients across an inverted hyperextended rift system: Example of the Mauléon Fossil Rift (Western Pyrenees). *Tectonics* 39(10).
- Schmandt B, Clayton RW. 2013. Analysis of teleseismic P-waves with a 5200-station array in Long Beach, California: Evidence for an abrupt boundary to Inner Borderland rifting. *J. Geophys. Res.* 118: 1–19 <https://doi.org/10.1002/jgrb.50370>.
- Schoeffler J. 1982. Les transversales basco-landaises. *Bull. Cent. Rech. ELF-Aquitaine* 6: 257–263.
- Shapiro N, Ritzwoller M. 2002. Monte-carlo inversion for a global shear-velocity model of the crust and upper mantle. *Geophysical Journal International* 151(1): 88–105.
- Shapiro NM, Campillo M, Stehly L, Ritzwoller MH. 2005. High-resolution surface-wave tomography from ambient seismic noise. *Science* 307: 1615–1618.
- Socco LV, Boiero D. 2008. Improved Monte Carlo inversion of surface wave data. *Geophysical Prospecting* 56(3): 357–371.
- Souriau A, Pauchet H. 1998. A new synthesis of Pyrenean seismicity and its tectonic implications. *Tectonophysics* 290: 221–244.
- Tarantola A, Valette B. 1982. Generalized nonlinear inverse problems solved using the least squares criterion. *Reviews of Geophysics* 20(2): 219–232.
- Teixell A, Labaume P, Lagabrielle Y. 2016. The crustal evolution of the west-central Pyrenees revisited: Inferences from a new kinematic scenario. *Comptes Rendus Geoscience* 348(3-4): 257–267.
- Teixell A, Labaume P, Ayarza P, Espurt N, de Saint Blanquat M, Lagabrielle Y. 2018. Crustal structure and evolution of the Pyrenean-Cantabrian Belt: A review and new interpretations from recent concepts and data. *Tectonophysics* 724: 146–170.
- Thomson WT. 1950. Transmission of elastic waves through a stratified solid medium. *Journal of Applied Physics* 21(2): 89–93. American Institute of Physics.
- Tryggvason A, Rognvaldsson S, Flovenz O. 2002. Three-dimensional imaging of the P- and S-wave velocity structure and earthquake locations beneath Southwest Iceland. *Geophysical Journal International* 151(3): 848–866.
- Tugend J, Manatschal G, Kuszniir NJ, Masini E, Mohn G, Thion I. 2014. Formation and deformation of hyperextended rift systems: Insights from rift domain mapping in the Bay of Biscay-Pyrenees. *Tectonics* 33(7): 1239–1276.
- Tugend J, Manatschal G, Kuszniir N. 2015. Spatial and temporal evolution of hyperextended rift systems: Implication for the nature, kinematics, and timing of the Iberian-European plate boundary. *Geology* 43(1): 15–18.
- Vacher P, Souriau A. 2001. A three-dimensional model of the Pyrenean deep structure based on gravity modelling, seismic images and petrological constraints. *Geophysical Journal International* 145(2): 460–470.
- Van Hinsbergen DJ, Torsvik TH, Schmid SM, Matenco LC, Maffione M, Vissers RL, *et al.* 2020. Orogenic architecture of the Mediterranean region and kinematic reconstruction of its tectonic evolution since the Triassic. *Gondwana Research* 81: 79–229.
- Vielzeuf D, Kornprobst J. 1984. Crustal splitting and the emplacement of Pyrenean Iherzolites and granulites. *Earth and Planetary Science Letters* 67(1): 87–96.
- Villaseñor A, Chevrot S, Sylvander M, Polychronopoulou K, Martakis N, Collin M, *et al.* 2019. Crustal architecture of the Mauléon Basin (Western Pyrenees) from high resolution local earthquake tomography using the large-N Maupasacq experiment. *Geophysical Research Abstracts*, vol. 21, *EGU General Assembly*.
- Waldner M, Bellahsen N, Mouthereau F, Bernet M, Pik R, Rosenberg CL, *et al.* 2021. Central Pyrenees Mountain building: Constraints from new It thermochronological data from the axial zone. *Tectonics* 40(3): e2020TC006614.
- Wang Y, Chevrot S, Monteiller V, Komatitsch D, Mouthereau F, Manatschal G, *et al.* 2016. The deep roots of the Western Pyrenees revealed by full waveform inversion of teleseismic P-waves. *Geology* 44(6): 475–478.
- Xia J, Miller R, Park C. 1999. Estimation of near-surface shear-wave velocity by inversion of Rayleigh waves. *Geophysics* 64(3): 691–700.

Zhang X, Curtis A, Galetti E, de Ridder S. 2018. 3-D Monte Carlo surface wave tomography. *Geophysical Journal International* 215 (3): 1644–1658.

Zolnai G. 1975. Sur l'existence d'un réseau de failles de décrochement dans l'avant-pays nord des Pyrénées occidentales. *Rev. Géogr. Phys. Géol. Dynam. Fr.* 17: 219–238.

**Cite this article as:** Lehujeur M, Chevrot S, Villaseñor A, Masini E, Saspiturry N, Lescoutre R, Sylvander M. 2021. Three-dimensional shear velocity structure of the Mauléon and Arzacq Basins (Western Pyrenees), *BSGF - Earth Sciences Bulletin* 192: 47.